Climate Dynamics (2022) 59:331–355
https://doi.org/10.1007/s00382-021-06129-5

Effects of the surface coupling strength in the WRF/Noah-MP model on regional climate simulations over China

Xia Zhang[1,2] · Liang Chen[1] · Zhuguo Ma[1,2] · Jianping Duan[1] · Danqiong Dai[1,2] · Haoxin Zhang[3]

Received: 7 February 2021 / Accepted: 29 December 2021 / Published online: 8 January 2022

Abstract

Land–atmosphere energy and moisture exchange can strongly influence local and regional climates. However, high uncertainty exists in the representation of land–atmosphere interactions in numerical models. Parameterization of surface exchange processes is greatly affected by parameter C_{zil}, which, however, is typically defined as a domain-wide constant value. In this study, we examine the sensitivity of regional climate simulations over China to different surface exchange strengths via three C_{zil} schemes (default (without C_{zil}), constant ($C_{zil}=0.1$), and dynamic canopy-height-dependent C_{zil}-h schemes) within a 13-km-resolution Weather Research and Forecasting model coupled with the Noah land surface model with multiparameterization options (WRF/Noah-MP). Our results demonstrate that compared to the other two schemes, the C_{zil}-h scheme substantially reduces land–atmosphere coupling strength overestimation, and comparison to Chinese terrestrial ecosystem flux research network (ChinaFLUX) observations reveals the capability of the C_{zil}-h scheme to better match observed surface energy and water variations. The results of the application of the various C_{zil} schemes in four typical climate zones in China demonstrate that the C_{zil}-h simulations achieve the closest agreement with field observations. The C_{zil}-h scheme can narrow the positive discrepancies in the simulated precipitation and surface fluxes and the negative biases of the land surface temperature in Northeast China, North China, eastern Northwest China, and Southwest China. In particular, the above remarkable improvements produced by the C_{zil}-h scheme primarily occur in areas covered with short vegetation. Additionally, the precipitation simulated with the C_{zil}-h scheme exhibits more intricate and uncertain changes compared with surface flux simulations due to the nonlocal impacts of the surface exchange strength resulting from atmospheric fluidity. Overall, our findings highlight the applicability of the dynamic C_{zil} scheme as a better physical alternative to the current treatment of surface exchange processes in atmosphere coupling models.

Keywords Land–atmosphere coupling · Surface exchange coefficient · Canopy-height-dependent C_{zil} · Surface fluxes · Climate zones

1 Introduction

Land–surface processes can play significant roles in cloud formation and precipitation generation (Findell and Eltahir 2003; Trier et al. 2004) by controlling energy, momentum, and mass transport to the lower atmosphere and subsequently affecting local planetary boundary layer profiles and differential surface heating (Betts et al. 1996; Los et al. 2006). The influences of local land surface characteristics such as land use, soil, and topography on precipitation occurrence and development are manifested especially in regions of strong land–atmosphere coupling (Houze 2012; Koster et al. 2003, 2004; Li et al. 2017; Pielke 2001; Zhang et al. 2020). For example, previous studies of the midwestern US drought in 1988 and flood in 1993, suggested that soil moisture (SM) conditions help to sustain extreme circumstances throughout the summer (Atlas et al. 1993; Trenberth and Guillemot 1996). These studies have underlined that land–atmosphere interactions may hold the key for improvement of weather forecasts and climate predictions.

✉ Liang Chen
chenliang@tea.ac.cn

[1] Key Laboratory of Regional Climate-Environment Research for Temperate East Asia, Institute of Atmospheric Physics, Chinese Academy of Sciences, Beijing, China

[2] University of Chinese Academy of Sciences, Beijing, China

[3] State Key Laboratory of Severe Weather and Institute of Tibetan Plateau and Polar Meteorology, Chinese Academy of Meteorological Sciences, Beijing, China

Land–atmosphere coupling has been investigated in many observational and modeling studies, such as the calculation of land–atmosphere feedback levels based on the atmospheric moisture budget (Trenberth 1999), diagnosis of a multimodel integrated coupling coefficient (Koster et al. 2004), and assessment of the relationship between SM, evaporation, and precipitation (Dirmeyer et al. 2006; Ruiz-Barradas and Nigam 2005; Zhang et al. 2008). However, there remain high uncertainties due to the complexity of coupling processes and their strong dependence on model or reanalysis results (Koster et al. 2003, 2004; Seneviratne et al. 2010). For instance, regions of notable coupling between summer rainfall and SM in observations could not be correctly captured in the Global Land–Atmosphere Coupling Experiment due to the unreliable performance of land surface models (LSMs) in capturing the coupling strength (Dirmeyer et al. 2006; Koster et al. 2004). Similarly, Zhang et al. (2008) reported that the central United States could not be identified as a region of strong coupling between precipitation and SM in their regional simulations. Furthermore, Ruiz-Barradas and Nigam (2005) demonstrated that excessive land–atmosphere coupling in numerical models produced an excessive latent heat flux (LH), resulting in potentially incorrect feedback between SM and precipitation. These studies emphasized the critical importance of proper land–atmosphere coupling representation in atmospheric models.

The surface exchange coefficient (C_h) denotes the efficiency of energy and moisture exchange between the land surface and atmosphere and controls the coupling strength in atmospheric models (Garratt 1992; LeMone et al. 2008). Current studies (e.g., Chen et al. (1997); Chen and Zhang (2009); Gan et al. (2019); Gomez et al (2020)) have indicated that C_h potentially constitutes a major uncertainty affecting model performance, but theoretical C_h parameterization remains poorly understood. Over recent decades, there have been many theoretical and experimental studies on C_h parameterization in which many efforts have been invested into the treatment of the surface roughness length of heat or moisture (Z_{ot}) and momentum (Z_{om}) (Brutsaert 1982; Chen et al. 1997; Chen and Zhang 2009; Yang et al. 2008). The roughness length describes the characteristics of surface fields combining the effects of land cover, orography and airflow. However, differences in transfer mechanisms, i.e., heat or moisture transport through molecular diffusion and momentum transport through pressure fluctuation gradients, generate discrepancies between Z_{ot} and Z_{om} (Reijmer et al. 2004; Rigden et al. 2018). Beljaars and Viterbo (1994) suggested that employing a fixed Z_{om}/Z_{ot} ratio of 10 could contribute to improvement in the simulated surface sensible heat flux (SH) and land surface temperature (T_s). Zilitinkevich (1995) created an empirical coefficient C_{zil} to bridge the relationship between Z_{ot} and Z_{om}. Chen et al. (1997) recommended applying the Zilitinkevich equation with $C_{zil}=0.1$, which yields results similar to the application of $Z_{om}/Z_{ot}=10$ in most cases, but the former nonfixed formulation is physically preferable and helps reduce the forecast precipitation bias. Thereafter, $C_{zil}=0.1$ in Zilitinkevich's formulation has been commonly implemented in National Centers for Environmental Prediction (NCEP) operational prediction systems. Furthermore, Chen and Zhang (2009) proposed a vegetation type-dependent C_{zil} that could achieve more realistic application of models in terms of land–atmosphere coupling representation.

Recent studies have been limited to the responses of land–surface processes to C_h parameterization but have ignored the extent to which C_h scheme variation can truly improve regional climate simulations. The importance of surface roughness in land–surface processes affecting the atmosphere has been frequently studied, e.g., the numerical experiments of Maynard and Royer (2004) demonstrated that a reduced surface roughness plays a dominant role in African tropical deforestation affecting climate change. Therefore, it is necessary to explore the sensitivity of climate change to parameter C_h, which heavily relies on the surface roughness and directly reflects the strength of land–atmosphere coupling. Additionally, C_h parameterization with a dynamic C_{zil} parameter provides more applications for evaluation studies in North America (e.g., Chen and Zhang (2009); Chen et al. (2019); Zheng et al. (2015)), but C_h evaluation in China has been conducted in only a few investigations confined to changes in land–surface processes and small areas, such as individual arid and semiarid sites (Chen et al. 2010; Yang et al. 2008) and the Yangtze River basin (Huang et al. 2016). The empirical C_{zil} coefficient contributes the most to the uncertainty in surface energy flux estimates (Siemann et al. 2018), and coefficient specification affects areas of strong land–atmosphere coupling in both location and strength (Zheng et al. 2015). Therefore, although investigations regarding the effects of a dynamic C_{zil} coefficient on surface flux and precipitation simulations at the point or regional scale (e.g., Chen et al. (2010); Huang et al. (2016); Trier et al. (2011)) have been conducted, C_h parameterization still exhibits a high uncertainty and sensitivity to changes in C_{zil} over regions spanning various topography, land-cover, and climate change conditions, especailly in China. Certain issues regarding proper coupling strength parameterization and the influence on surface flux and regional climate simulations should be further explored.

The objective of this study is to assess the variability in regional climate simulations in response to the representation of land–atmosphere coupling in numerical models, and to provide potential mechanisms explaining this variability. In contrast to previous studies directly adjusting C_{zil} values in the Chen97 scheme (e.g., Chen and Zhang (2009); Huang et al. (2016); Zheng et al. (2015)), we introduced the Zilitinkevich equation with a dynamic C_{zil} coefficient

into the Monin–Obukhov (M–O) scheme (hereafter referred to as C_{zil}-h) using the Weather Research and Forecasting model (WRF) coupled with the Noah LSM with multiparameterization options (Noah-MP) (WRF/Noah-MP). Section 2 describes the detailed land–atmosphere coupling method and the experimental setup involving the coupled WRF/Noah-MP model. Section 3 assesses the capability of C_{zil}-h in improving land–atmosphere coupling and its impacts on regional climate simulations. In Sect. 4, the uncertainty in the C_{zil}-h scheme is examined in regional climate modeling. Conclusions are outlined in Sect. 5.

2 Methodology, model and data

2.1 Land–atmosphere coupling method

The Noah-MP LSM provides lower boundary layer conditions for the planetary boundary layer scheme in the coupled atmospheric WRF model (Chen et al. 2007; Skamarock et al. 2008), which relies on the surface fluxes of SH and LH (unit: W m^{-2}), as determined through the following bulk transfer equations (Garratt 1992):

$$\mathrm{SH} = \rho C_p C_h |U| \left(\theta_s - \theta_a\right), \tag{1}$$

$$\mathrm{LH} = \rho C_e |U| \left(q_s - q_a\right), \tag{2}$$

where ρ is the air density (kg m^{-3}), C_p is the air heat capacity (J kg^{-1} K^{-1}), and U is the wind speed (m s^{-1}). Moreover, θ_a and q_a are the potential temperature (K) and specific humidity (kg kg^{-1}), respectively, of air and θ_s and q_s are the potential temperature (K) and specific humidity (kg kg^{-1}), respectively, at the surface. C_h (unitless) is the surface exchange coefficient for SH, and C_e is the surface exchange coefficient for LH. Many studies (e.g., Högström (1967); Swinbank and Dyer (1967)) have concluded a general equivalency between C_e and C_h based on the observed high correlation between the air temperature (T_a) and specific humidity over evaporating surfaces, and this approximation has been widely adopted in numerical models (e.g., Chen et al. (1997); Huang et al. (2016); Trier et al. (2011)). Therefore, this study focuses on C_h parameterization, which is directly linked to the coupling strength and controls the inputs of the total energy flux into the lower atmosphere. Observed C_h values can be reconstituted from measurements of the variables contained in the following equation (Chen and Zhang 2009):

$$C_h = \frac{\mathrm{SH}}{\rho C_p |U| \left(\theta_s - \theta_a\right)}. \tag{3}$$

Instruments at stations directly provided SH and U data, θ_a was converted from T_a observations adiabatically adjusted for the height above the surface, and θ_s was estimated from the upwelling longwave radiation following the Stephan-Boltzmann relationship (Yang et al. 2008). C_p and ρ values can be derived from T_a, relative humidity, and surface pressure observations (Allen et al. 1998; Goff 1957).

Regarding the M–O scheme within the Noah-MP LSM, C_h is parameterized as a function of the roughness length based on the M–O similarity theory (Brutsaert 1982), as follows:

$$C_h = \frac{k^2}{\left[\ln\left(\frac{Z-d_0}{z_{om}}\right) - \psi_m\left(\frac{Z-d_0}{L}\right)\right]\left[\ln\left(\frac{Z-d_0}{z_{ot}}\right) - \psi_h\left(\frac{Z-d_0}{L}\right)\right]}, \tag{4}$$

$$L = -\frac{\rho C_p u_*^3 T_{\mathrm{ah}}}{k \cdot g \cdot \mathrm{SH}}, \tag{5}$$

where Z is the height above the ground surface (m), d_0 is the zero-displacement height (m), L is the M–O length (m), and the $(Z\text{-}d_0)/L$ ratio is denoted as the nondimensional M–O stability parameter ζ. In addition, T_{ah} is the canopy air temperature (K), u_* is the friction velocity (m), $k = 0.4$ is the von Kaman constant, and $g = 9.8$ m s^{-2} is the gravitational acceleration. Moreover, Ψ_m is the momentum stability function, Ψ_h is the heat stability function (Paulson 1970), Z_{om} is the aerodynamic roughness length (m), denoting the height at which the extrapolated wind speed reaches zero, and Z_{ot} is the thermal roughness length (m), representing the height at which the extrapolated T_a equals T_s.

Z_{ot} can be related to Z_{om} through an atmospheric flow function, as proposed by Zilitinkevich (1995), as follows:

$$Z_{\mathrm{ot}} = Z_{\mathrm{om}} \exp\left(-kC_{\mathrm{zil}}\sqrt{R_e}\right) \text{ and } R_e = \frac{u^* Z_{\mathrm{om}}}{\upsilon}, \tag{6}$$

where C_{zil} is an empirical coefficient, v is the kinematic molecular viscosity ($\sim 1.5 \times 10^{-5}$ m^2 s^{-1}), and R_e is the roughness Reynolds number. C_{zil} values are usually assumed to range from 0.01 to 1.0, with surface coupling varying from strong to weak (Chen et al. 1997; Zheng et al. 2015). C_{zil} in the current versions of the WRF model is assigned a value of 0.1 based on earlier model comparisons and calibrations against field data (Chen et al. 1997), but only the Chen97 option provides access to the default C_{zil} value of 0.1 because the M–O option assumes $Z_{\mathrm{ot}} = Z_{\mathrm{om}}$ without considering C_{zil}.

Furthermore, a dynamic vegetation type-dependent C_{zil} scheme was proposed by Chen and Zhang (2009), and multiyear Ameriflux data and the least squares regression method were employed to determine parameter C_{zil} as a function of the canopy height h (unit: m):

$$C_{zil} = 10^{(-0.4h)}. \quad (7)$$

2.2 Coupled WRF/Noah-MP model and experimental design

In this study, the WRF 3.9.1 model coupled with Noah-MP (WRF/Noah-MP) was applied to investigate the sensitivity of regional climate simulations to land–atmosphere coupling. As a state-of-the-art atmospheric modeling system, the WRF model (Skamarock et al. 2008) contains full physical processes and multiple parameterization options and thus usually functions as a common framework applied to physical scheme improvement, regional climate simulation, and numerical weather prediction. The Noah-MP LSM (Niu et al. 2011), the successor of the Noah LSM (Chen et al. 1996), is applied as an augmented land surface module in the coupled WRF model. Similar to the WRF model, multiple physics scheme options are available in Noah-MP.

The WRF/Noah-MP experiments in this study were initiated at 00:00 UTC on 1 February and ran until 00:00 UTC on 1 September (i.e., the vegetation growing season) between 2003 and 2012, in which the first month of each year was treated as the model spin-up time. As shown in Fig. 1a, the model was integrated over a domain covering the entire China land surface with a central point located at 37° N and 102.5° E. The horizontal resolution was 13 km with 399 × 344 grid points. The grid vertically contained 36 terrain-following eta levels with the model top occurring at 100 hPa. Atmospheric lateral boundary conditions and initial atmospheric fields were retrieved from 6-hourly 0.75° × 0.75° European Centre for Medium-Range Weather Forecast Interim Reanalysis (ERA-Interim) data (Dee et al. 2011).

The physical parameterization schemes employed in this study include the Noah-MP LSM (Niu et al. 2011), Thompson microphysics (Thompson et al. 2008), Kain-Fritsch convection (Kain 2004), Yonsei University planetary boundary layer (Hong et al. 2006), and rapid radiative transfer models (Iacono et al. 2008). The Noah-MP LSM provides two options to calculate C_h: the M–O (Brutsaert 1982) and Chen97 (Chen et al. 1997) schemes. Both of these options are based on the M–O similarity theory and heavily rely on the aerodynamic (Z_{om}) and thermal (Z_{ot}) roughness lengths and atmospheric stability. The primary differences lie in the treatment of the roughness length, i.e., the Chen97 scheme accounts for the discrepancy between Z_{ot} and Z_{om} through parameter C_{zil} (usually $C_{zil} = 0.1$, so $Z_{ot} = Z_{om}/10$), while the M–O scheme considers identical roughness lengths but the zero-displacement height. In this study, we performed model experiments by incorporating the Z_{om}/Z_{ot} relationship of Eq. (6) with the dynamic C_{zil} coefficient of Eq. (7) into the M–O scheme.

Three cases were designed to simulate the different responses of regional climate simulations to land–atmosphere coupling: Case 1 (Default; $C_{zil} \sim 0$) adopted the original M–O option to calculate C_h, Case 2 (C_{zil}; $C_{zil} = 0.1$) adopted a typical constant C_{zil} value, and Case 3 (Newczil; C_{zil}-h) adopted a dynamic canopy height dependent C_{zil}.

2.3 Validation datasets

Surface meteorological data (V3.0), including over 2000 stations from 2003 to 2012 operated by the China Meteorological Administration (CMA), were utilized to derive regional C_h observations and verify the model performance. The variables involved include hourly precipitation and T_a as well as T_s, surface wind speed, surface humidity and surface pressure at 6-hourly intervals. With the use of Cressman-type interpolation, we horizontally interpolated the on-site observations to obtain gridded data at the 399 × 344 grid points, which exhibited the same resolution as that of the regional climate simulations. The SH data required to calculate C_h observations were obtained from the monthly 0.0833° FLUXNET-Model Tree Ensemble (MTE) dataset provided by the Max Planck Institute for Biogeochemistry. The gridded FLUXNET-MTE dataset was integrated considering 253 global FLUXNET eddy covariance observations and the MTE machine learning algorithm (Jung et al. 2009). FLUXNET-MTE products have been widely employed as a proxy for observations in analysis of land–atmosphere energy exchange and validation of land surface modeling at regional and global scales (Bonan et al. 2011; Gan et al. 2019; Zhang et al. 2019). It should be noted that this gridded dataset provides no values in areas of western China due to the lack of observation stations, and the unevenly distributed flux towers considered to train the model tree can create nonnegligible uncertainty in the product. Additionally, we collected measurements at eight flux tower sites (Table 1) from the Chinese terrestrial ecosystem flux research network (ChinaFLUX) to reconstruct C_h and evaluate surface energy and water simulation variations. The collected 30-min flux observations were located in areas spanning different land-cover types (grasslands, forestlands, and wetlands) and climatic regimes (arid, semiarid, semihumid, and wet climatic regions).

In addition, the atmospheric aridity index (AI), which is the ratio of the annual accumulated precipitation to the potential evapotranspiration, was utilized to determine dry and wet climatic regions (Hulme 1996; Middleton and Thomas 1992). AI values were derived using monthly 0.5° precipitation and potential evapotranspiration data from 1983 to 2012 in the Climate Research Unit (CRU)-TS3.23 dataset acquired from the University of East Anglia. Extreme arid, arid, semiarid, semiarid and semihumid, and humid climate zones were defined according to $0 \le AI < 0.05$, $0.05 \le AI < 0.20$, $0.20 \le AI < 0.50$, $0.50 \le AI < 0.65$, and $AI \ge 0.65$, respectively.

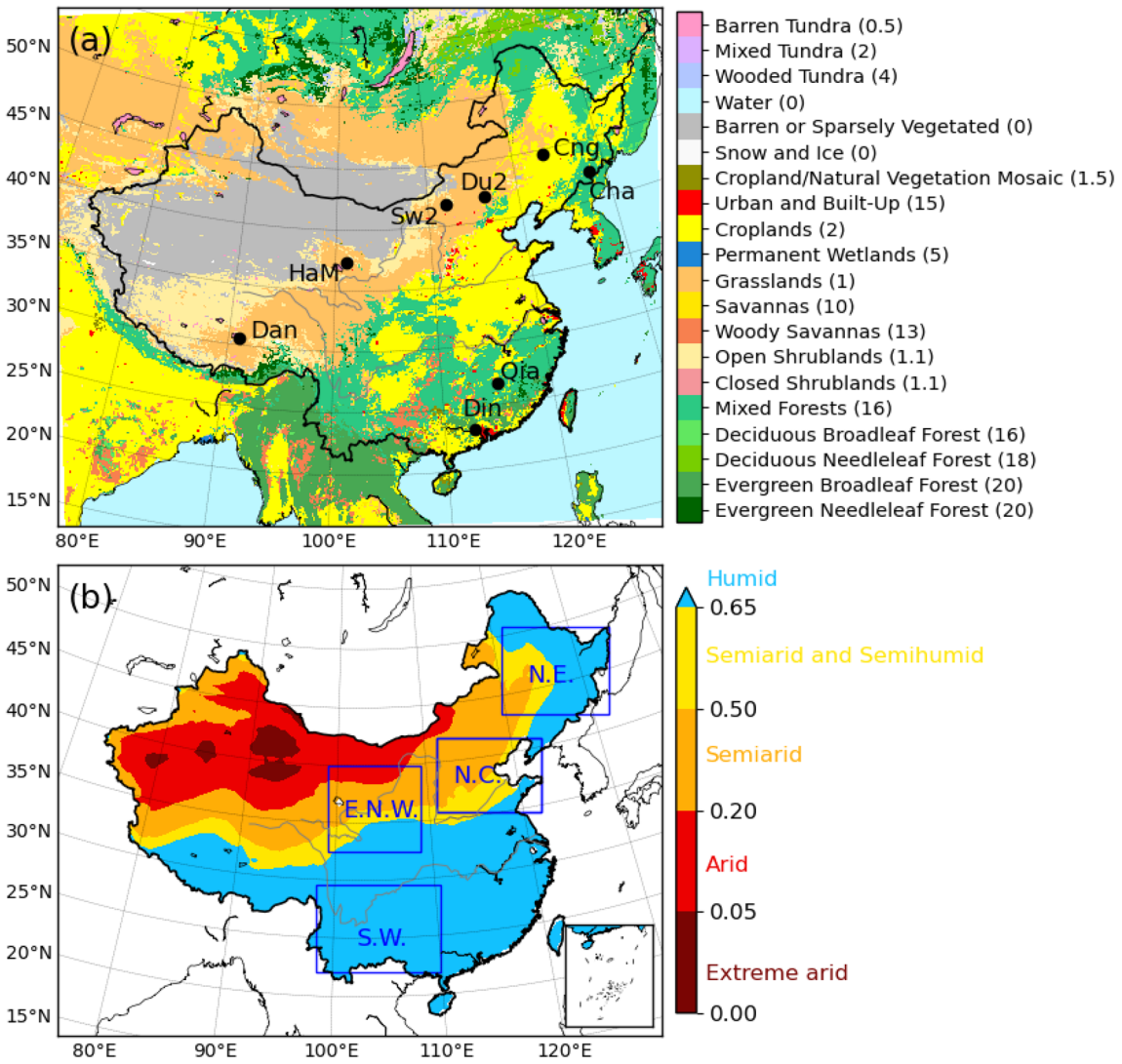

Fig. 1 **a** Weather Research and Forecasting model coupled with the Noah land surface model with multiparameterization options (WRF/Noah-MP) modeling domain. The shaded contours indicate Moderate Resolution Imaging Spectroradiometer (MODIS) land cover/land use classification data within the International Geosphere-Biosphere Program (IGBP). The values in parentheses indicate the canopy height (unit: m). The dark circles denote the locations of the eight ChinaFLUX sites: Changbaishan (Cha), Changling (Cng), Dangxiong (Dan), Dinghushan (Din), Duolun (Du2), Haibei Alpine (HaM), Qianyanzhou (Qia), and Siziwang Banner (Sw2). **b** Division of wet and dry climate zones in China. The shaded contours indicate the atmospheric aridity index, which is the ratio of the annual accumulated precipitation to the potential evapotranspiration. The blue rectangles indicate the four typical climate regions selected in this study. NE: Northeast China (120–135° E, 42.5–50° N); NC: North China (110–123° E, 35–41° N); ENW: eastern Northwest China (99–109° E, 32.5–40° N); SW: Southwest China (98–111°E, 22–28°N)

3 Results

3.1 Model verification

Prior to employing the WRF model to explore the characteristics and influences of land–atmosphere coupling on the local climate, the model skill was examined considering available field observations. Here, we evaluated default M–O simulations against on-site observations in terms of T_a and precipitation. Three statistics commonly considered to quantify the consistency between model outputs and field observations [e.g., Brovkin et al. (2013); Dai et al. (2019)] were adopted, namely, the Pearson correlation coefficient, mean bias error, and root mean square error (RMSE).

Figure 2 shows that the simulated summer T_a and precipitation patterns agreed well with those of the observations across China from 2003 to 2012, with spatial correlations of 0.86 and 0.78, respectively. The simulated T_a pattern could capture the observed large-scale pattern, although

Table 1 General information on the eight ChinaFLUX sites considered in this study

Site code	Site name	Latitude, longitude	Elevation (m)	Land-cover type	Canopy height (m)	Years
CN-Cng	Changling	44.59, 123.51	270	GRA	0.17	2008
CN-Dan	Dangxiong	30.50, 91.07	4250	GRA	0.1	2004–2005
CN-Du2	Duolun	42.05, 116.28	1324	GRA	0.3	2007
CN-HaM	Haibei Alpine	37.37, 101.18	3190	GRA	0.25	2003
CN-Sw2	Siziwang Banner	41.79, 111.90	1456	GRA	0.1	2011
CN-Cha	Changbaishan	42.40, 128.10	738	MF	26	2003–2005
CN-Din	Dinghushan	23.17, 112.54	240	EBF	17	2003–2005
CN-Qia	Qianyanzhou	26.74, 115.06	100	ENF	12	2003–2005

GRA grasslands, *WET* permanent wetlands, *ENF* evergreen needleleaf forestlands, *EBF* evergreen broadleaf forestlands, *MF* mixed forestlands

colder simulation values occurred in the southwest of China and warmer simulation values occurred in the northwest of China. The modeled precipitation pattern resembled to the observed pattern involving small rainfall amounts in the northwest and large rainfall amounts in the southeast, despite an overestimated magnitude observed in most areas. Furthermore, the model capacity for the simulation of the temporal evolution of T_a and precipitation was assessed in four typical climate regions in China (the blue rectangles in Fig. 1b). As shown in Fig. 3, the model reproduced the observed T_a and precipitation variability levels well and mostly yielded significantly positive correlations higher than 0.8 exceeding the 95% confidence level. However, the simulations in Northeast China, North China, and Southwest China exhibited cold biases, while those in eastern Northwest China tended to exhibit warm biases. Additionally, the model generated excessive rainfall in these four regions, especially in Southwest China, with a large positive deviation, which may be attributed to the influences of the Asian summer monsoon and plateau topography (Song et al. 2010; Wang et al. 2014). Accurate T_a and precipitation estimation has remained a challenge. In particular, general precipitation overestimation has occurred with many atmospheric models (Liu et al. 2017; Wang et al. 2015). The simulation accuracy could be

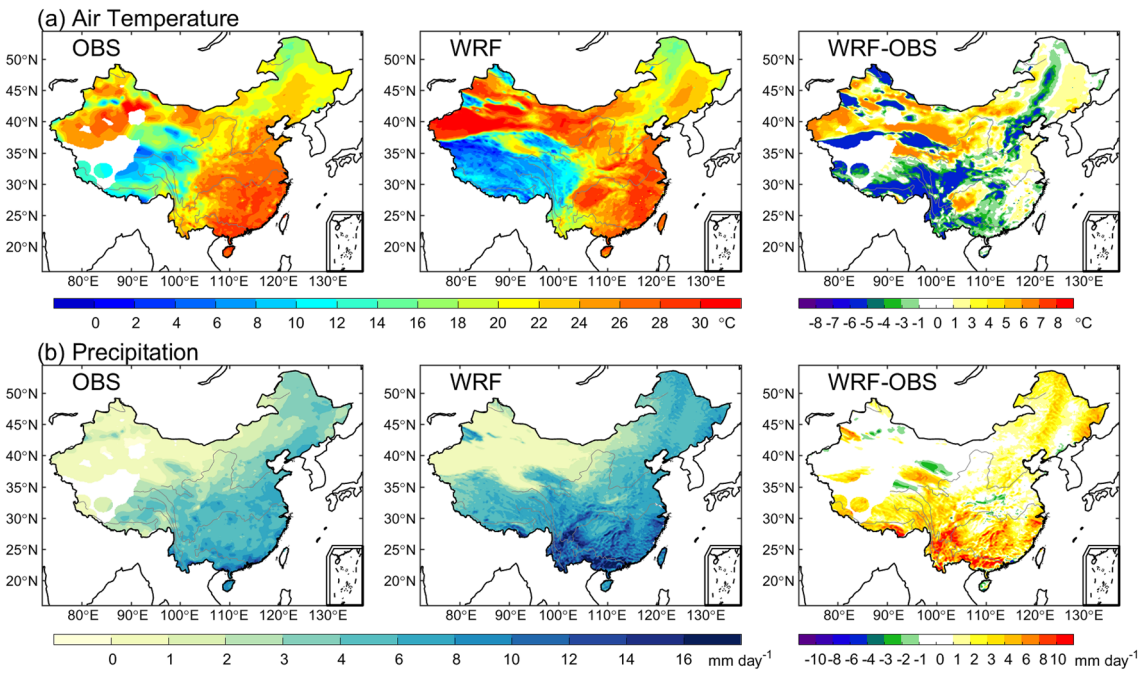

Fig. 2 Spatial patterns of **a** the near-surface air temperature and **b** precipitation in the field observations retrieved from the China Meteorological Administration (OBS) and the simulations with the WRF/Noah-MP model using the default M–O scheme (WRF), in addition to the differences (WRF-OBS) in summer from 2003 to 2012

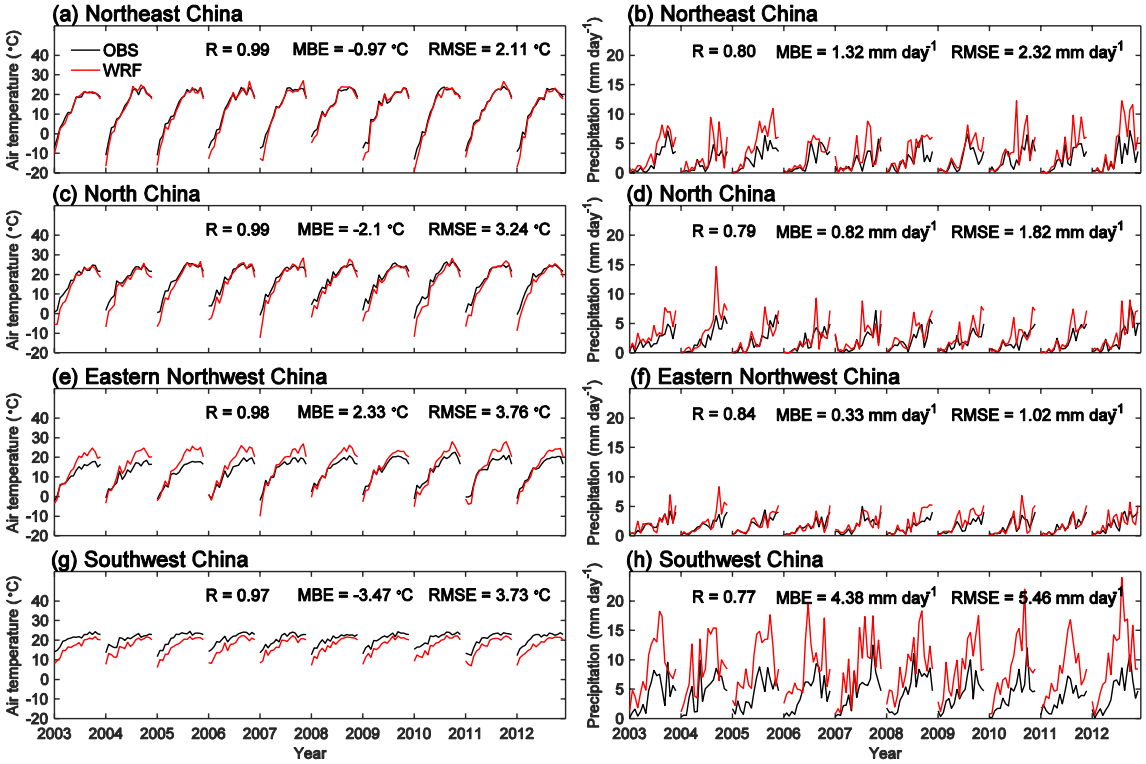

Fig. 3 Temporal evolution of the near-surface air temperature and precipitation in the field observations obtained from the China Meteorological Administration (OBS) and the simulations with the WRF/Noah-MP model using the default M–O scheme (WRF) for **a**, **b** Northeast China, **c**, **d** North China, **e**, **f** eastern Northwest China and **g**, **h** Southwest China from March to August during the 2003–2012 period. R, MBE, and RMSE denote the Pearson correlation coefficient, mean bias error, and root mean square error, respectively

improved through the reduction in errors in model boundary conditions and further development of critical physical parameterizations, e.g., boundary layer and radiative transfer schemes for T_a simulation (Wang and Zeng 2011; Wang et al. 2015) and cloud microphysical and cumulus schemes for precipitation simulation (Gao et al. 2020; Liu et al. 2017).

In general, the WRF model employed in this study exhibits a good performance in capturing the features and temporal evolution of observed large-scale spatial patterns, and verification analysis has indicated that WRF model application in sensitivity experiments can provide helpful information regarding the modification characteristics of the regional climate under different coupling strength extents.

3.2 Impacts of C_{zil} on the land–atmosphere coupling strength

The various C_{zil} schemes adopted in surface layer parameterization through the exchange efficiency of land–atmosphere energy and moisture may produce pronounced effects on the evolution of weather and climate systems (Chen and Zhang 2009; LeMone et al. 2008; Trier et al. 2011). Therefore, we first comparatively analyzed the simulated C_h in the different C_{zil} experiments based on field observations prior to assessing the impacts of land–atmosphere coupling on the regional climate.

C_h observations were calculated with Eq. (3) based on surface flux and meteorological measurements. Figure 4a–c shows general overestimations in most areas of China in 2003–2012 summers over observation-derived C_h values. Considering Fig. 4a–c and d, e, the C_{zil}-h scheme generally produced the closest C_h values with the observations and remarkably reduced the positive C_h bias in the default M–O and $C_{zil}=0.1$ experiments, which suggests improvement in the application of the dynamic C_{zil} scheme in representing land–atmosphere coupling. Furthermore, the C_h simulations exhibited notable variability across the various vegetation types. As shown in Fig. 4f, a large increase in C_h from a smooth sparsely vegetated surface with short canopies to a rough densely vegetated surface with high canopies occurred, as revealed by the observations. Particularly, the C_{zil}-h scheme performed the best in areas covered by short vegetation (e.g., barren, crop, grassland, and shrubland areas) with the smallest mean bias error of 0.37 and exhibited a similar behavior of coupling strength modification to that of the default M–O scheme in grids with tall vegetation (e.g., mixed forestland areas), thereby producing overestimated but reasonable C_h values.

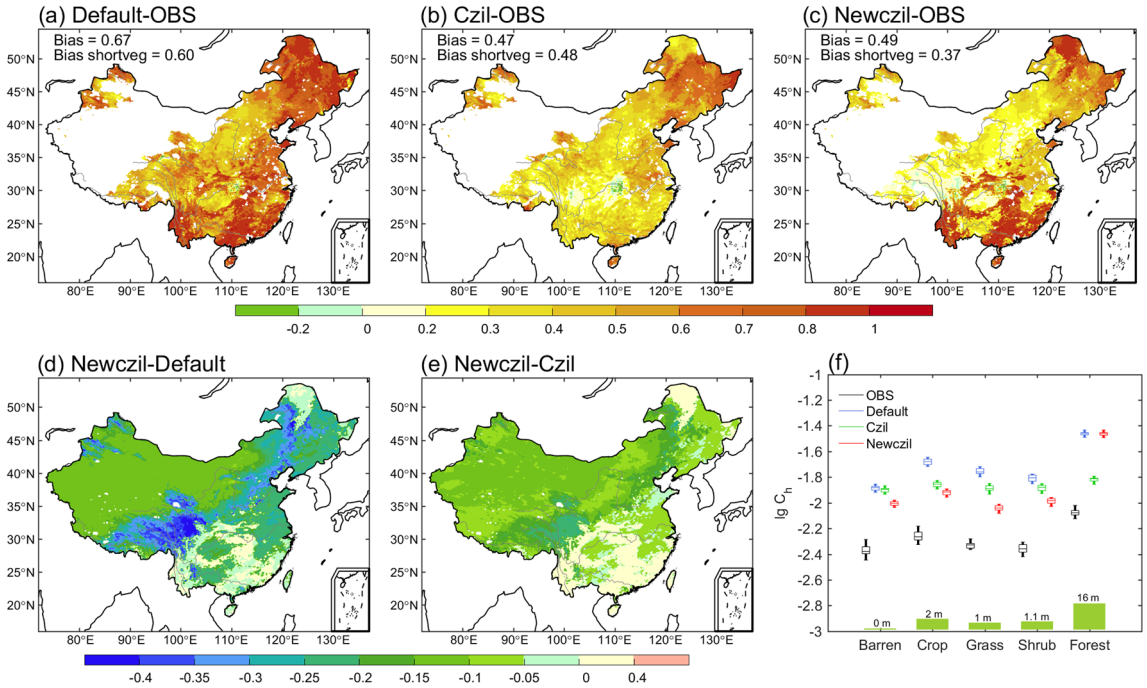

Fig. 4 Comparisons of the surface exchange coefficient, C_h (plotted at a log10 scale), derived from the field observations of the China Meteorological Administration (OBS), and calculated with the WRF/Noah-MP model using the default M–O (Default), $C_{zil}=0.1$ (Czil), and C_{zil}-h (Newczil) schemes in summer from 2003 to 2012. **a**–**c** Differences between the simulations and observations, **d**, **e** differences between the simulations, and **f** regional averaged C_h values for the typical land-cover types. Bias: the mean deviation in the simulations from the observations; Bias shortveg: the discrepancy between the simulated and observed values averaged over short vegetation areas with canopy heights < 5 m. The green bars in **f** indicate the canopy height

The results in this study are generally consistent with the findings obtained using offline Noah-MP simulations over China (Zhang et al. 2021) and employing FLUXNET observations and numerical models in North America (Chen and Zhang 2009; Chen et al. 2019). Overall, the adopted C_{zil}-h scheme can help improve the representation of land–atmosphere coupling in coupled atmospheric models and thus influence land–atmosphere energy and moisture transport. Hence, this study next focuses on the extent of the influence of these processes on surface and atmospheric conditions.

3.3 Impacts of C_{zil} on surface energy and water variations

The land–atmosphere coupling (C_h) representation in the atmospheric model was verified to be improved by the C_{zil}-h scheme in Sect. 3.2. Furthermore, the potential skill of the C_{zil}-h scheme in replicating the observed surface energy and water components was evaluated. Figure 5 shows the daily evolution trends of SH, LH, soil temperature (ST), and SM averaged over the ChinaFLUX grassland sites (Cng, Dan, Du2, HaM, and Sw2; Table 1) and forestland sites (Cha, Din, and Qia) from March to August. ST and SM were simulated in four soil layers (0–0.1, 0.1–0.4, 0.4–1, and 1–2 m), and the observed values were measured at 0.05 m except at the Sw2 site (0−0.3 m). The simulated ST and SM were aggregated to match the observed soil layer. The model could favorably capture the daily variability in the observed surface energy and water fluxes. However, the SH, LH, ST, and SM values were generally overestimated in all C_{zil} experiments. In contrast, the simulations involving the C_{zil}-h scheme agreed better with the measurements at the ChinaFLUX grassland sites, with minimum RMSE values for SH, LH, and ST of 14.55 W m^{-2}, 18.38 W m^{-2}, and 1.41 °C, respectively. The various C_{zil} schemes produced minor differences in the simulated SM values. Furthermore, the diurnal surface heat fluxes at the ChinaFLUX grassland and forestland sites are shown in Fig. 6. The different C_{zil} schemes yielded larger SH and LH diurnal amplitudes in the simulations than those reflected in the flux measurements, especially during the daytime. However, the C_{zil}-h scheme substantially reduced the obtained SH overestimation with the default M–O and $C_{zil}=0.1$ schemes, which corresponds to the effect of the C_{zil}-h scheme in weakening excessively strong coupling (Fig. 4). Comparatively, the modeled LH values with the

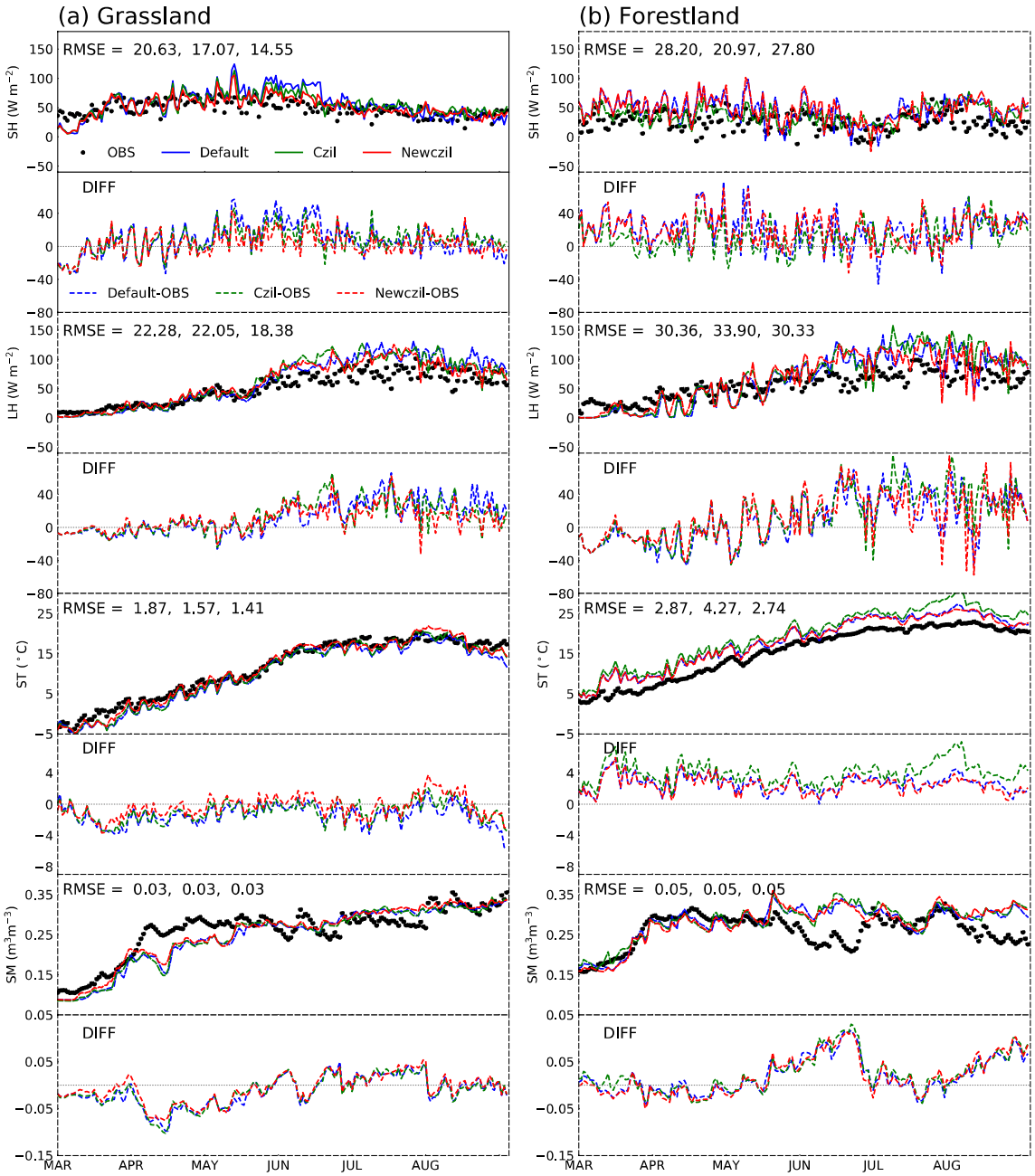

Fig. 5 Comparisons of the daily sensible heat flux (SH), latent heat flux (LH), soil temperature (ST), and soil moisture (SM) from March to August between the ChinaFLUX observations (OBS) and the WRF/Noah-MP simulations using the default M–O (Default), C_{zil}=0.1 (Czil), and C_{zil}-*h* (Newczil) schemes. The values in **a** are averaged over the ChinaFLUX grassland sites (Cng, Dan, Du2, HaM, and Sw2) in the respective available years (Table 1), and the values in **b** are averaged over the forestland sites (Cha, Din, and Qia). The root mean square errors (RMSEs) for the default M–O, C_{zil}=0.1, and C_{zil}-*h* simulations are sequentially displayed in each panel

three C_{zil} schemes exhibited negligible discrepancies in both grassland and forestland areas.

3.4 Responses of the regional climate simulations to C_{zil} in the four typical climate zones of China

Thus far, we demonstrated that the C_{zil}-*h* scheme contributed significantly to improvement in the WRF/Noah-MP model performance in representing land–atmosphere coupling and

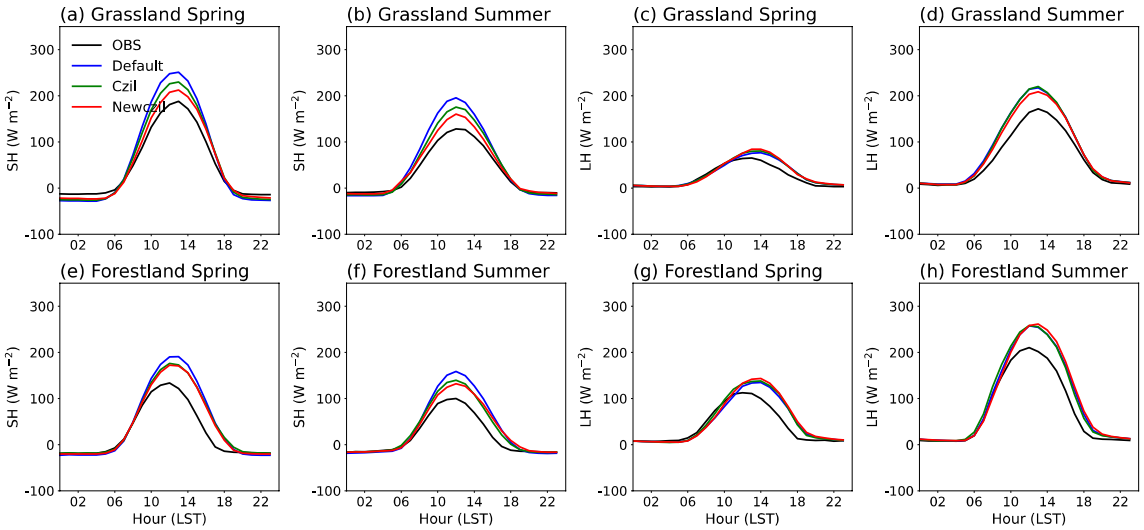

Fig. 6 Diurnal comparisons of the sensible heat flux (SH) and latent heat flux (LH) between the ChinaFLUX observations (OBS) and the WRF/Noah-MP simulations using the default M–O (Default), $C_{zil}=0.1$ (Czil), and C_{zil}-h (Newczil) schemes. The values in **a**–**d** are averaged over the ChinaFLUX grassland sites (Cng, Dan, Du2, HaM, and Sw2) in the respective available years (Table 1), and the values in **e**–**h** are averaged over the forestland sites (Cha, Din, and Qia)

regenerating surface fluxes. Furthermore, the C_{zil}-h scheme was applied to four typical climate zones in China (the blue rectangles in Fig. 1b), and the behavior in replicating the observed regional climate was assessed. Northeast China, North China, and eastern Northwest China are located in dry–wet transition zones with notable land–atmosphere interactions (Huang et al. 2017; Li et al. 2017; Ma and Fu 2003) and predominantly covered with short vegetation (e.g., crop and grass), and Southwest China located in a humid zone was primarily chosen because of the high coverage of tall vegetation (e.g., mixed forestland).

Figure 7 shows the differences in summertime precipitation between the simulations involving the three C_{zil} schemes and the CMA field observations from 2003 to 2012. The different C_{zil} schemes generally produced similar climatological precipitation spatial patterns but varying precipitation intensity levels. The simulated precipitation magnitudes were larger than those of the observations, whereas the C_{zil}-h scheme decreased the positive deviations in the simulations with the other two C_{zil} schemes and provided notable improvement in northeastern Northeast China, southern North China, southwestern and eastern Northwest China, and northeastern Southwest China. Compared to the default M–O and $C_{zil}=0.1$ simulations, the C_{zil}-h scheme reduced the warm T_a biases in eastern Northwest China and the cool T_s biases in Northeast China, North China and Southwest China (Figs. 8, 9), exhibiting minimal mean deviations from the CMA observations. Figures 10, 11 show the discrepancies in SH and LH between the WRF/Noah-MP simulations and the FLUXNET-MTE observations. The C_{zil}-h scheme generally narrowed the mean biases of the surface fluxes simulated with the other two C_{zil} schemes and attained a higher consistency with the observations. These features correspond to the skill of the C_{zil}-h scheme in significantly reducing the observed C_h overestimation with the default M–O and $C_{zil}=0.1$ schemes (Fig. 4). The C_{zil}-h scheme, through mitigation of the land–surface coupling efficiency (Fig. 4), transferred fewer surface heat fluxes into the atmosphere (Figs. 10, 11) and generated a corresponding increase in T_s (Fig. 9) and decrease in T_a (Fig. 8), which consequently occurred through the atmospheric planetary boundary layer affecting atmospheric precipitation (Fig. 7). Generally, with increasing precipitation, a high water availability results in a wetter land surface, leading to greater evaporative cooling and a subsequent reduction in the land–air temperature contrast (ΔT) (Lian et al. 2017; Mildrexler et al. 2011; Wang and Zeng 2011). Therefore, the reduced precipitation in the C_{zil}-h experiment (Fig. 7) in turn promoted a larger ΔT with increasing T_s (Fig. 9) and decreasing T_a (Fig. 8). Additionally, remarkable improvements in the four climate zones primarily occurred in the short vegetation areas with canopy heights < 5 m (Fig. 1a).

Atmospheric circulations affecting precipitation were analyzed through moisture fluxes and divergences vertically integrated from 1000 to 300 hPa (Fig. 12). The C_{zil} treatment in surface layer parameterization notably affects water vapor transport. The differences between the various C_{zil} simulations exhibited a distinct seasonality and regionality, with more remarkable moisture transport deviations in summer and over eastern China. The moisture divergence in the C_{zil}-h simulations increased over North China, eastern Northwest China, eastern Northeast China, and Southwest China

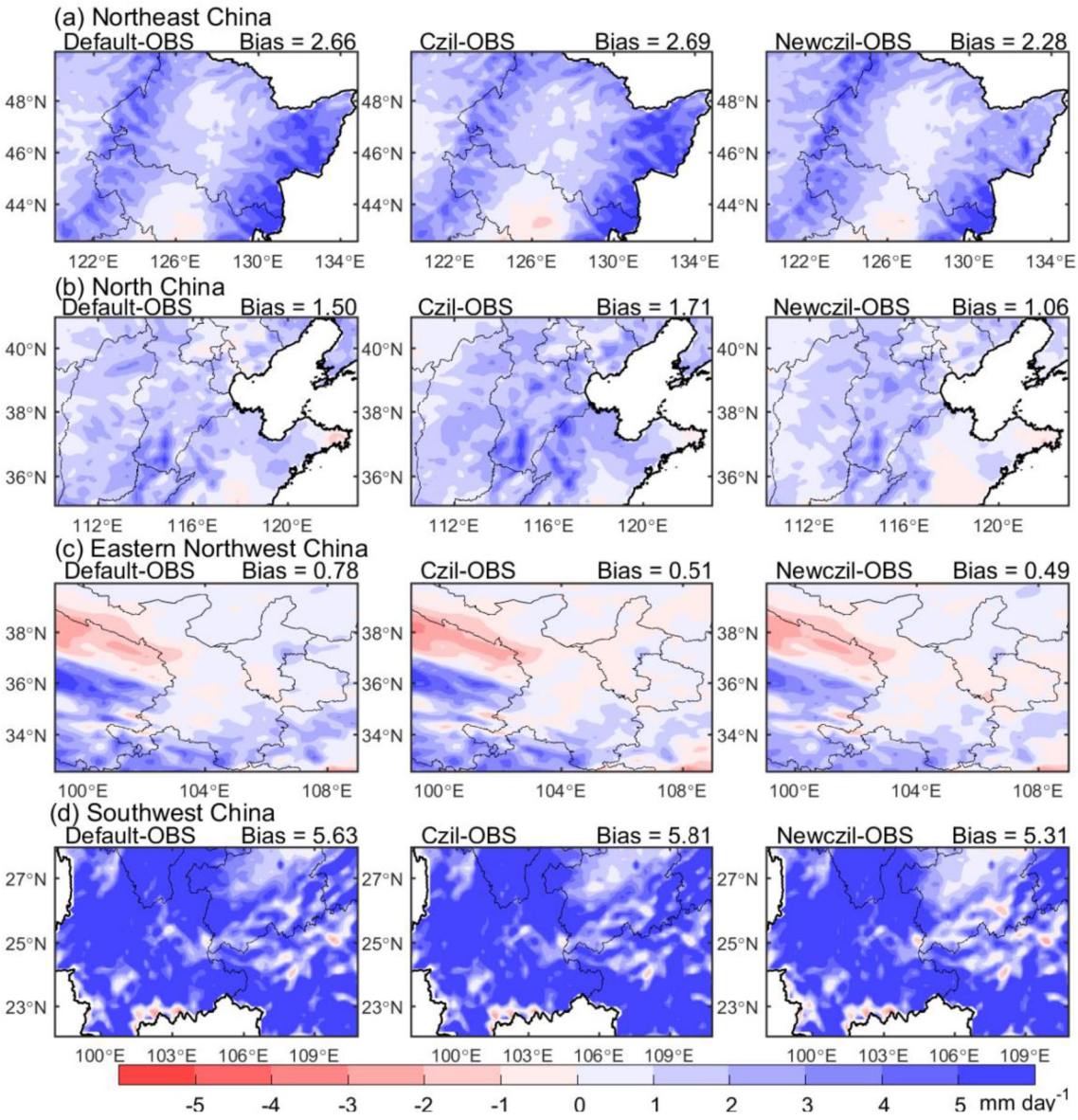

Fig. 7 Spatial differences in precipitation between the field observations retrieved from the China Meteorological Administration (OBS) and the WRF/Noah-MP simulations using the default M–O (Default), $C_{zil}=0.1$ (Czil), and C_{zil}-h (Newczil) schemes in **a** Northeast China, **b** North China, **c** eastern Northwest China and **d** Southwest China in summer from 2003 to 2012. Bias: the mean discrepancy between the simulations and observations

in summer (Fig. 12c, d), which indicates that the net water inflow decreased. Subsequently, as shown in Fig. 7, the C_{zil}-h scheme reduced the wet biases obtained in the precipitation simulations in the four regions. Additionally, atmospheric convective conditions in terms of the convective available potential energy (CAPE), planetary boundary layer height (PBLH), and 2-m specific humidity (Fig. 13) were analyzed to reveal the potential influence of convective activity on precipitation based on the different C_{zil} schemes. CAPE represents the amount of energy available for convection, and is an indicator of atmospheric instability. Compared to the default M–O and $C_{zil}=0.1$ schemes, the C_{zil}-h scheme considerably reduced the atmospheric instability energy over a wide area, which is unfavorable for the onset of convective triggering and precipitation occurrence. The elevated PBLH simulated with the C_{zil}-h scheme enhanced water vapor mixing in the lower atmosphere, in addition to greater water vapor evaporation due to a higher T_s (Fig. 9), leading to a conspicuous reduction in the near-surface humidity. These unfavorable convective conditions could potentially reduce the precipitation intensity in the C_{zil}-h experiments in the four climate zones. Additionally, significant CAPE changes

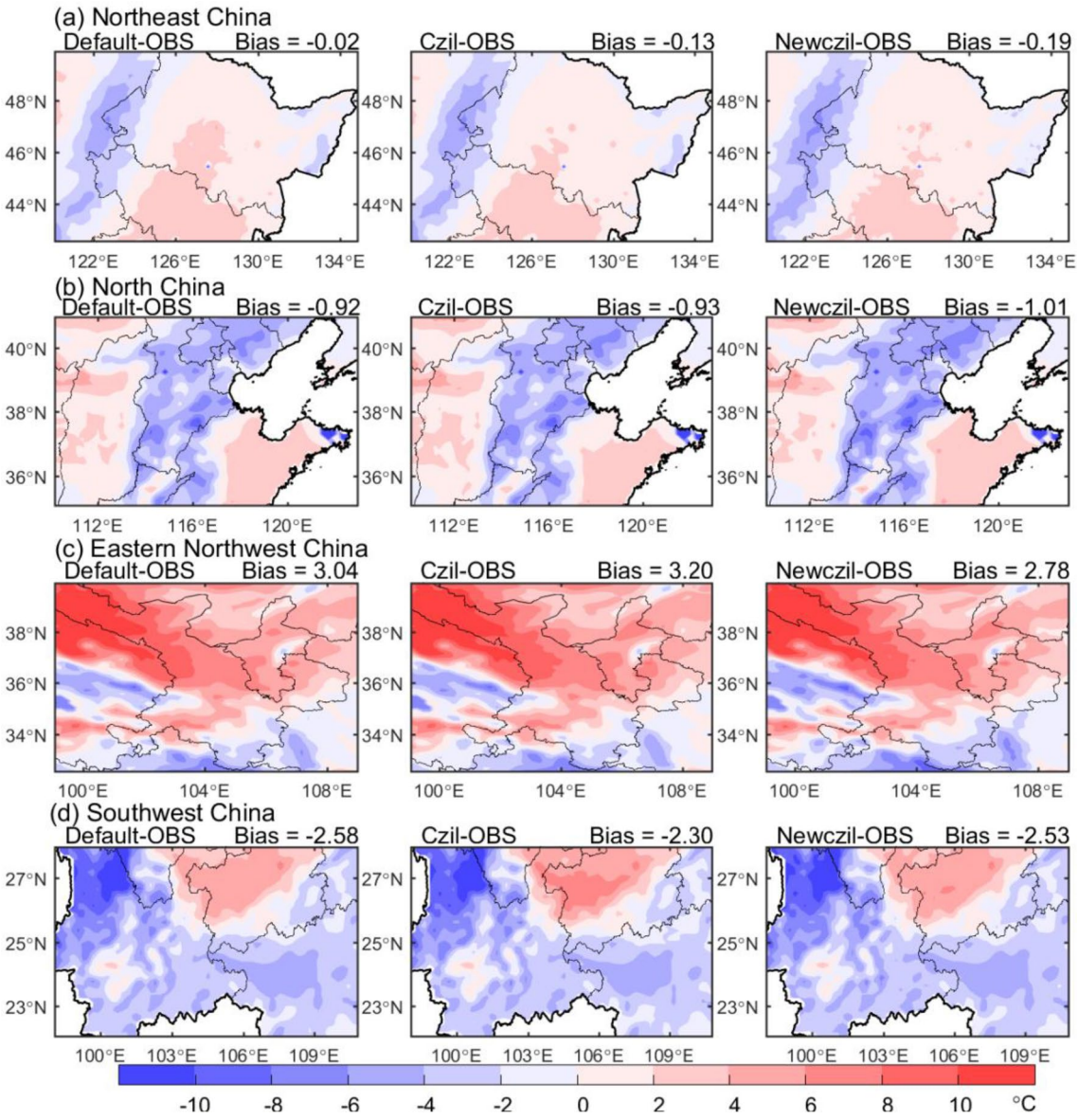

Fig. 8 Spatial differences in the near-surface air temperature between the field observations retrieved from the China Meteorological Administration (OBS) and the WRF/Noah-MP simulations using the default M–O (Default), $C_{zil}=0.1$ (Czil), and C_{zil}-h (Newczil) schemes in **a** Northeast China, **b** North China, **c** eastern Northwest China and **d** Southwest China in summer from 2003 to 2012. Bias: the mean discrepancy between the simulations and observations

potentially indicated a better representation of summer precipitation through convection-permitting modeling (Kurkute et al. 2020; Li et al. 2019; Liu et al. 2017). This inspired us to employ a convection-permitting model in future studies to explore the precipitation simulation improvements achievable with the C_{zil}-h scheme.

Previous studies (e.g., Huo et al. (2021); Koster et al. (2003); Li et al. (2018)) have reported that many factors in the Earth system influence precipitation changes and establish feedbacks between atmospheric processes and land surface fluxes. Similarly, the precipitation responses to the different C_{zil} schemes are complicated and do not exactly correspond to the obtained C_h variation patterns (Fig. 4). This suggests that the changes in surface heat fluxes driving the evolution process of the boundary layer alter atmospheric circulations and further affect the formation of clouds and precipitation (Trier et al. 2011; Zheng et al. 2015). Furthermore, to comprehensively understand the physical mechanisms of the changes in precipitation induced by the C_{zil}-h scheme, Table 2 quantitatively analyzes the differences

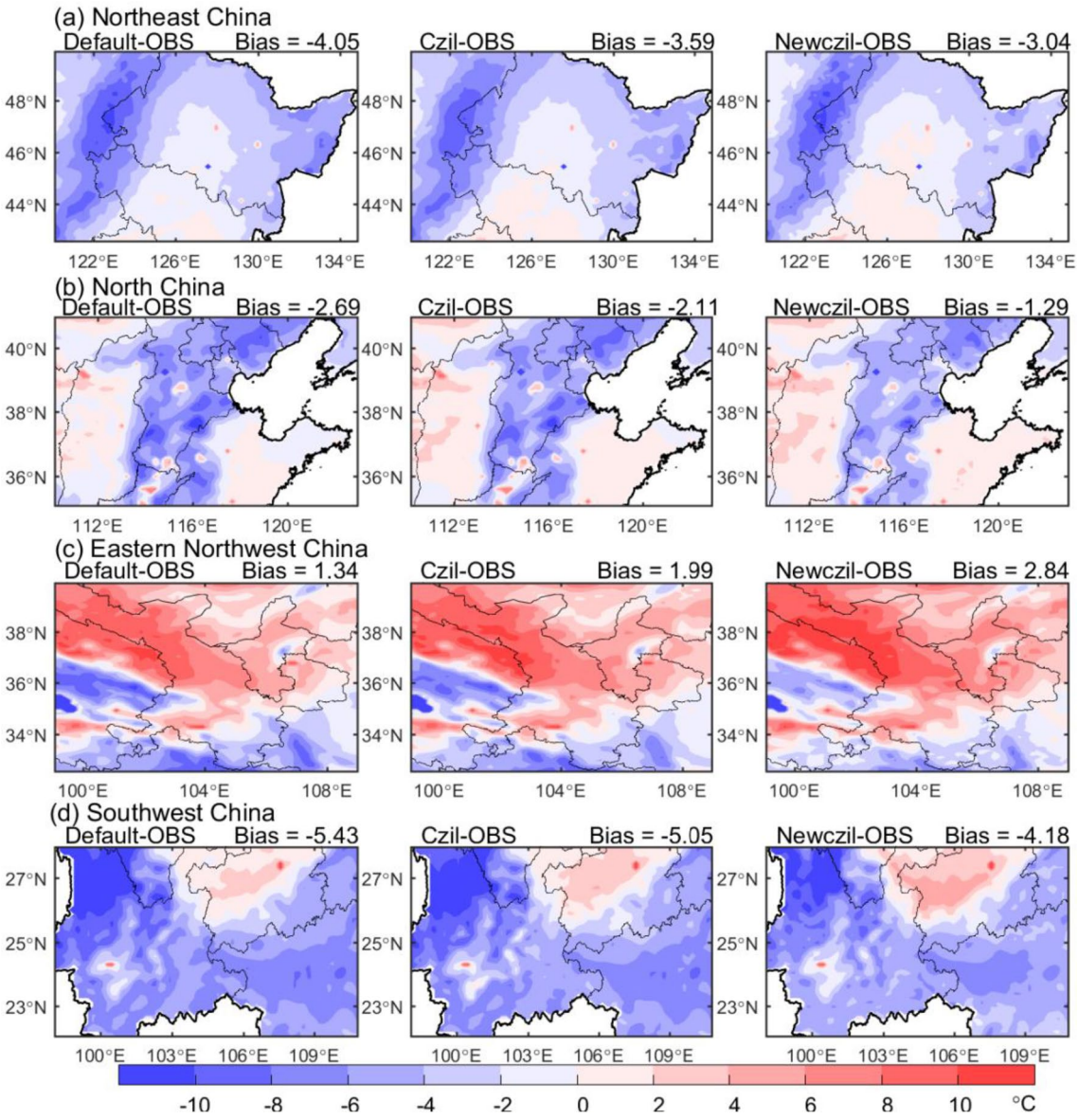

Fig. 9 Spatial differences in the land surface temperature between the field observations obtained from the China Meteorological Administration (OBS) and the WRF/Noah-MP simulations using the default M–O (Default), $C_{zil}=0.1$ (Czil), and C_{zil}-h (Newczil) schemes in **a** Northeast China, **b** North China, **c** eastern Northwest China and **d** Southwest China in summer from 2003 to 2012. Bias: the mean discrepancy between the simulations and observations

in simulations between the various C_{zil} schemes in the four climate zones by jointly considering thermal and dynamical factors. The C_{zil}-h scheme simulated less precipitation than did the default M–O scheme in Northeast China, North China, eastern Northwest China, and Southwest China in summer. The above decrease in precipitation is associated with horizontal transport of less water vapor from moisture source areas such as the Bay of Bengal and South China Sea (Table 2 and Fig. 12), evaporation of less water vapor from drier surfaces, thus vertically weakening LH, and stabilization of the lower atmosphere and thermal convection suppression due to a lower CAPE. The SH values decreased with decreasing coupling strength (C_h) in the C_{zil}-h experiments, which, along with lower surface heat fluxes transferred into the atmosphere, led to a large increase in T_s and a small decrease in T_a. A corresponding rise in ΔT caused PBLH deepening under thermal instability conditions. Additionally, clouds can inhibit shortwave radiation from reaching the surface (Huo et al. 2021; Molod et al., 2015). Therefore, less precipitation and fewer cloudy days contributed

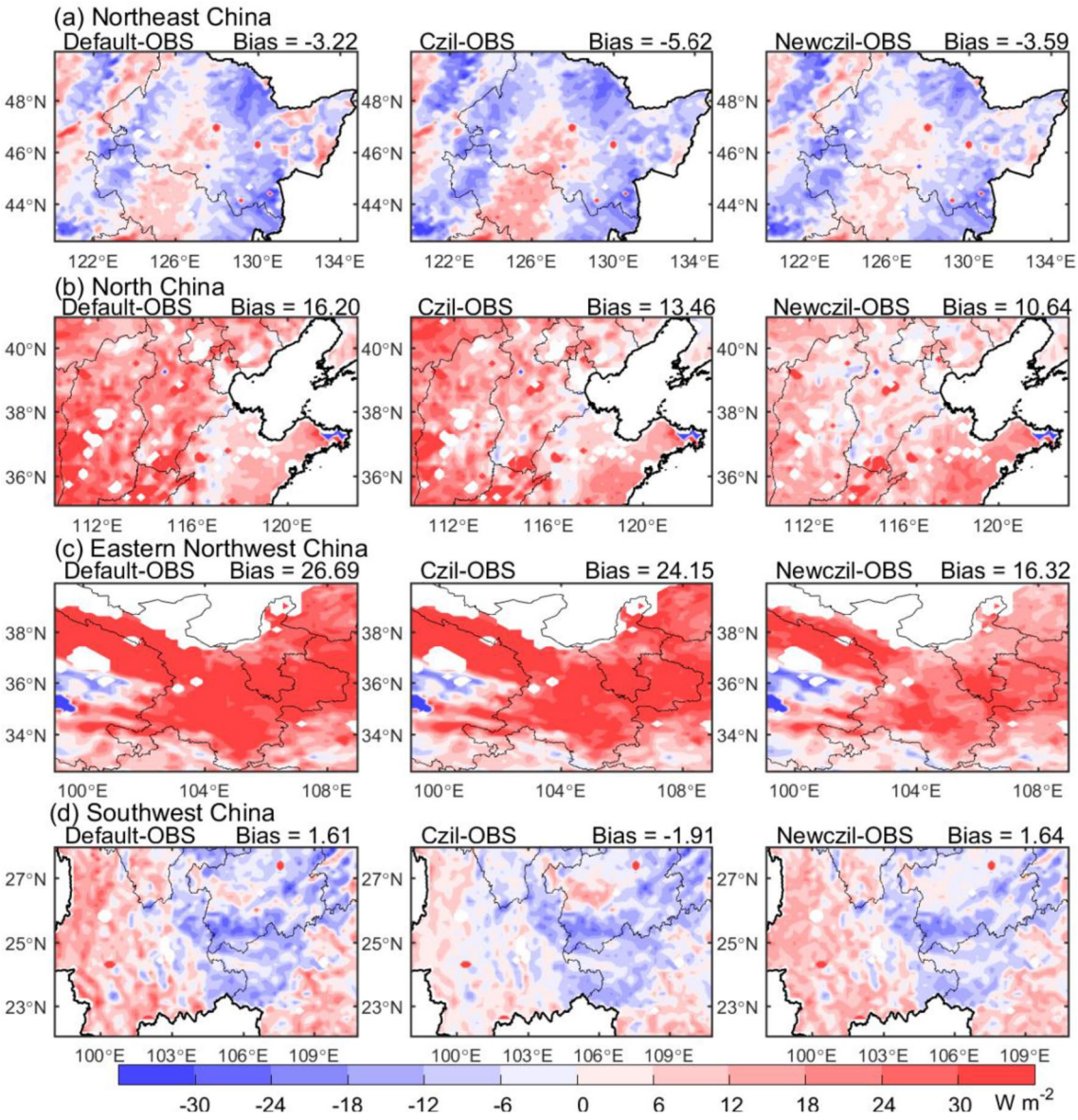

Fig. 10 Spatial differences in the sensible heat flux between the FLUXNET-MTE observations (OBS) and the WRF/Noah-MP simulations using the default M–O (Default), $C_{zil}=0.1$ (Czil), and C_{zil}-h (Newczil) schemes in **a** Northeast China, **b** North China, **c** eastern Northwest China and **d** Southwest China in summer from 2003 to 2012. Bias: the mean discrepancy between the simulations and observations

to the above PBLH deepening. Water vapor conditions can also notably contribute to PBLH changes by regulating the energy balance near the surface (Kurkute et al. 2020; Lian et al. 2017; Wang et al. 2015). The C_{zil}-h scheme generated intensified precipitation in spring, which corresponded to more water vapor available for precipitation from enhanced horizontal moisture transport, higher humidity and increased LH under favorable convective conditions. Compared to the $C_{zil}=0.1$ simulations, the C_{zil}-h scheme produced less precipitation across the four regions in summer and Northeast China and Southwest China in spring and increased precipitation amounts in North China and eastern Northwest China in spring. The responses of precipitation changes to the surface and atmospheric components simulated with the C_{zil}-h scheme against the $C_{zil}=0.1$ scheme were generally consistent with those simulated against the default M–O scheme.

Additionally, according to Table 2, the large discrepancies in ΔT between the C_{zil} simulations primarily arose from the contribution of T_s, and the T_a values varied slightly between the different C_{zil} schemes. For example, the difference in summer

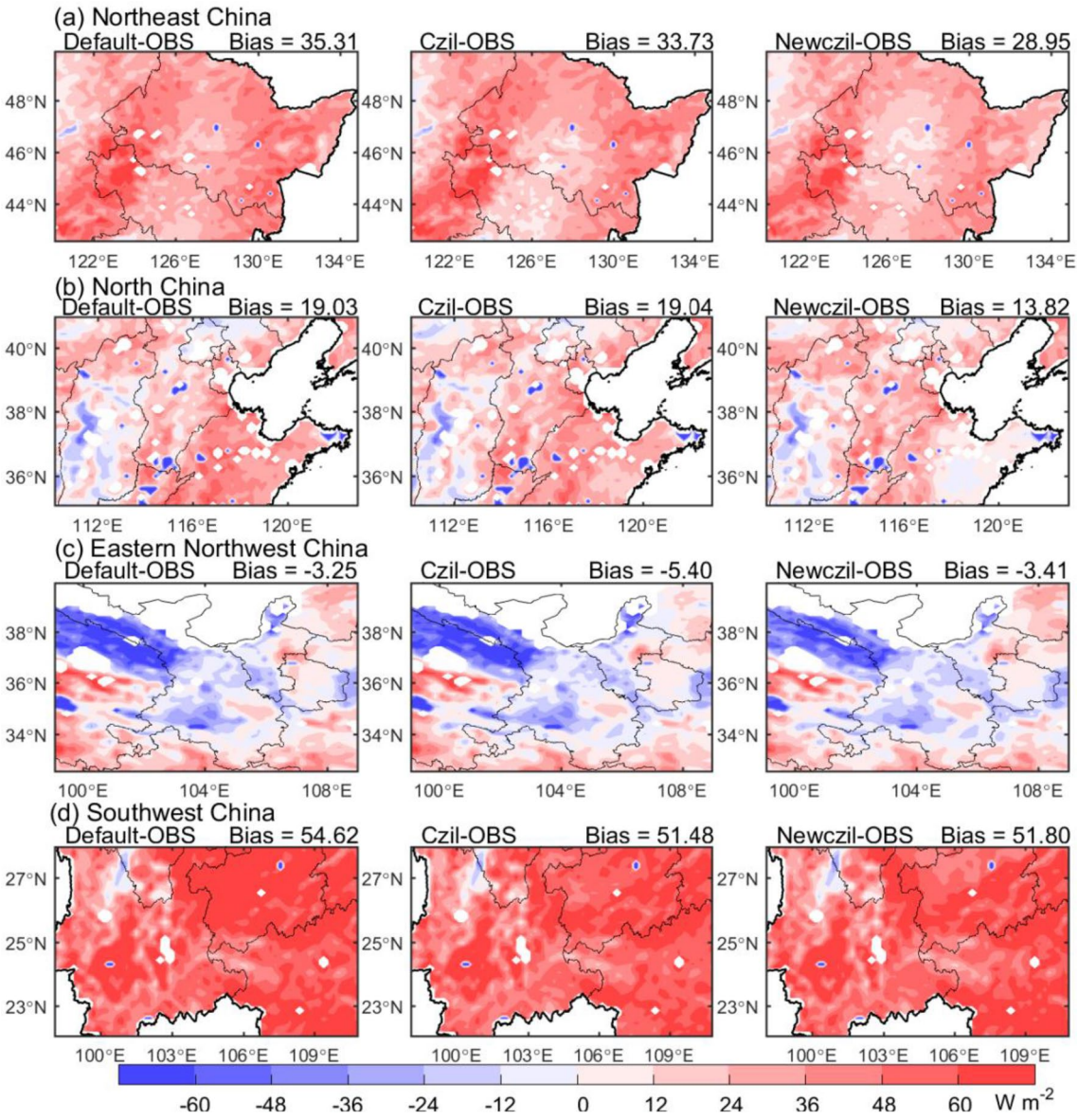

Fig. 11 Spatial differences in the latent heat flux between the FLUXNET-MTE observations (OBS) and the WRF/Noah-MP simulations using the default M–O (Default), $C_{zil}=0.1$ (Czil), and C_{zil}-h (Newczil) schemes in **a** Northeast China, **b** North China, **c** eastern Northwest China and **d** Southwest China in summer from 2003 to 2012. Bias: the mean discrepancy between the simulations and observations

ΔT in North China between the C_{zil}-h and default M–O schemes was 1.58 °C, in which the mean bias for T_s reached 1.39 °C (a contribution of 87.97%) and that for T_a reached −0.20 °C. These results demonstrate the important role of C_h in controlling T_s, and Yang et al. (2011) indicated that C_h is the most important factor in modeling T_s. Hence, considerable efforts by LSM modelers have invested to improve the model performance in reproducing T_s through C_h parameterization (Chen et al. 2011; Gomez et al. 2020).

4 Discussion

4.1 Sensitivity of the surface flux and precipitation simulations to the C_{zil}-h scheme and uncertainty in C_{zil}-h scheme application

In this study, we verified that C_{zil} in surface layer parameterization could be slightly adjusted with the WRF coupled model to improve regional climate simulations in China.

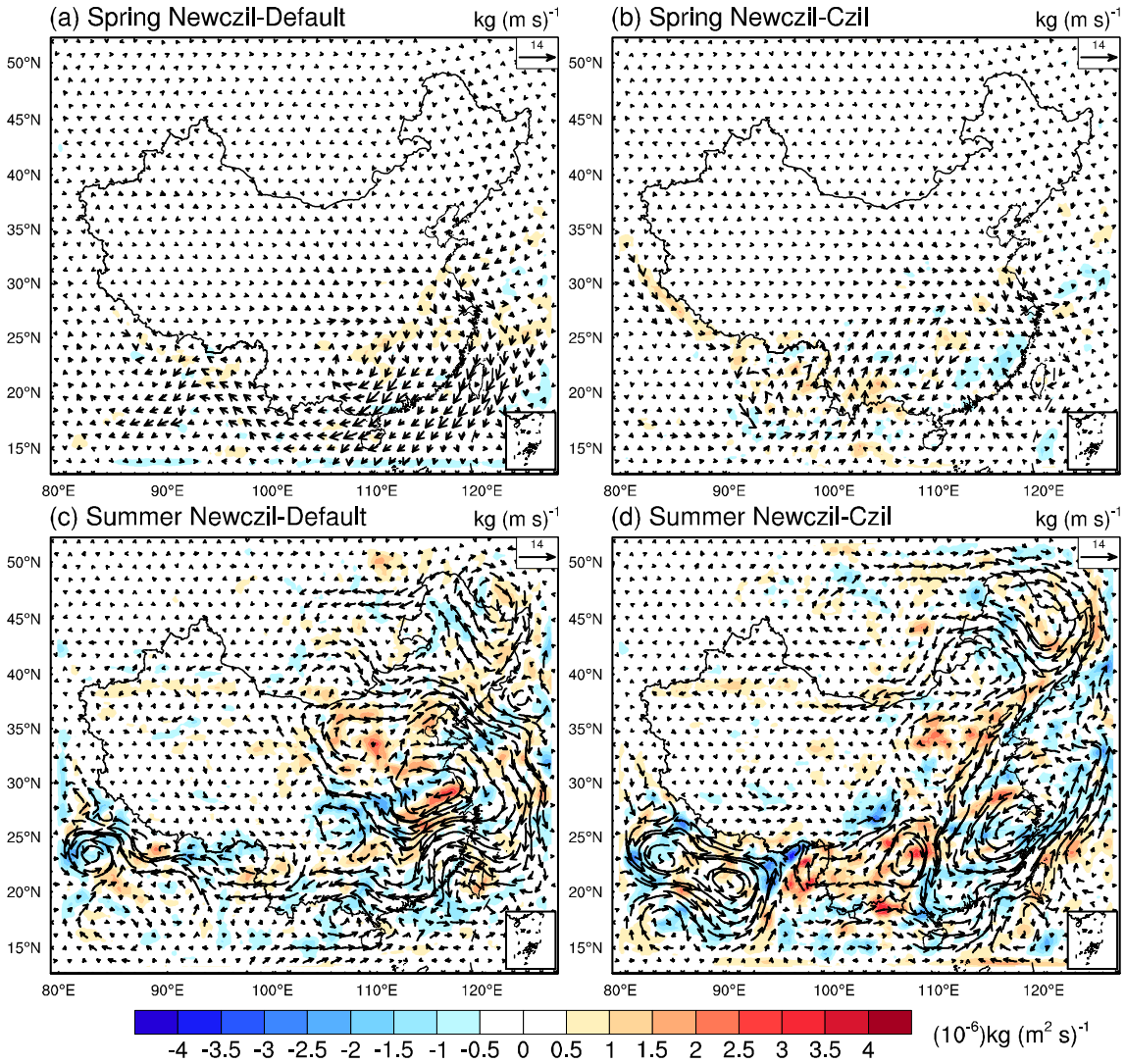

Fig. 12 Spatial difference in moisture flux transport (vector, unit: kg (m s)$^{-1}$) and moisture flux divergence (shading; unit: 10^{-6} kg (m^2 s)$^{-1}$) between the simulations using the default M–O (Default), C_{zil}=0.1 (Czil), and C_{zil}-h (Newczil) schemes in spring and summer from 2003 to 2012. The moisture flux values are derived by multiplying the specific humidity and vector wind and vertically integrated from 1000 to 300 hPa

Compared to the control experiments without considering C_{zil} or directly setting a constant value of 0.1, the dynamic C_{zil} scheme depending on the vegetation type (i.e., C_{zil}-h) could achieve improvements in simulating the land–atmosphere coupling strength, thus affecting the atmospheric planetary boundary layer through the exchange of heat and moisture and altering regional climate simulations. However, the impacts of the C_{zil}-h scheme on the simulations notably varied with the land-cover type, variables, and season, etc. Specifically, the C_{zil}-h scheme could reduce the observed overestimation in both the default M–O and C_{zil} = 1 experiments in regard to short vegetation canopies, but the C_{zil}-h scheme behaved similarly to the default M–O scheme in regard to high canopies. Furthermore, the behavior of the C_{zil}-h scheme was inconsistent among all surface and atmospheric variables. Therefore, this section quantifies the sensitivity of the simulations to the C_{zil}-h scheme by analyzing the discrepancies between the various C_{zil} experiments and examines the deficiencies of applying the C_{zil}-h scheme in numerical models.

Considering that the experiments designed in this study are greatly affected by the land-cover type, we analyzed C_h, SH, T_s and precipitation, which are strongly influenced by the different C_{zil} schemes, considering three dominant vegetation types in China. Figure 14 and Table 3 indicate the relative deviations between the simulations using the different C_{zil} schemes. The values for grasslands, croplands, and forestlands were extracted from eastern Northwest China,

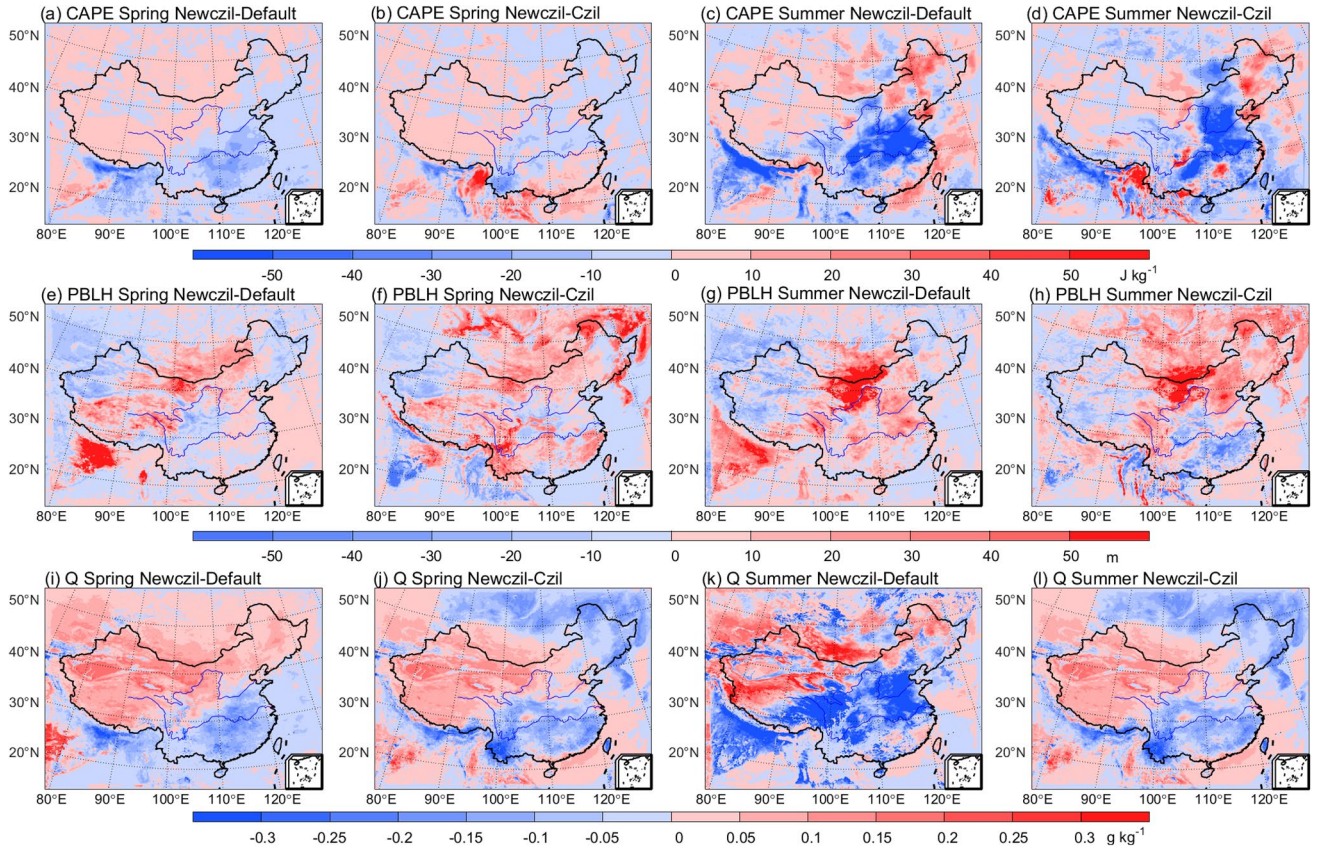

Fig. 13 Spatial differences in **a**–**d** the convective available potential energy (CAPE), **e**–**h** planetary boundary layer height (PBLH), and **i**–**l** 2-m air specific humidity (Q) between the simulations using the default M–O (Default), $C_{zil}=0.1$ (Czil), and C_{zil}-h (Newczil) schemes in spring and summer from 2003 to 2012

North China, and Southwest China, respectively (Fig. 1). A relative deviation in C_h of approximately −10% (−12%) between the C_{zil}-h and default M–O simulations occurred in grassland (cropland) areas, which was double (quadruple) the relative deviation between the C_{zil}-h and $C_{zil}=0.1$ simulations. These results indicate the marked influence of the C_{zil} coupling coefficient on the simulation results and the substantial reduction obtained with the C_{zil}-h scheme in the C_h overestimation generated by the default M–O scheme, corresponding to the results in Fig. 4. The C_{zil}-h scheme generated an average relative deviation of −8.12% in C_h over the control experiments for short vegetation canopies, and the weakened coupling strength resulted in reduced surface SH (an average relative deviation of −6.82%) inputs into the atmosphere and a higher T_s (an average relative deviation of 5.28%). The C_h simulations in the C_{zil}-h experiments at the forestland sites exhibited large positive deviations (relative deviation > 36%) against the $C_{zil}=0.1$ simulations, consequently resulting in significantly higher SH values (relative deviation > 16%) and negative T_s deviations (< −8%). The precipitation generated with the C_{zil}-h scheme in grassland and cropland areas produced a mean negative deviation of −4.69% over the control experiments. Although the C_h values simulated with the C_{zil}-h scheme in forestland areas exhibited small negative deviations (< 0.2%) against the default M–O scheme, these minor biases in the land–atmosphere coupling strength could result in distinctively different precipitation levels, especially in summer, with relative deviations reaching up to 60%. This probably occurs because local available moisture and energy are affected by the enhancement in land–atmosphere exchange efficiency as vegetation proliferates from spring to summer (Chen and Zhang 2009; Zhang et al. 2021) and the influence of horizontal moisture flux transport (Fig. 12).

Theoretically, the fundamental reason for the differences in the simulations between the various C_{zil} schemes is that the C_{zil}-h scheme can directly relate the surface coupling strength to terrestrial ecosystems through Eq. (7), thus affecting the Z_{om}/Z_{ot} ratio, which is critical in C_h calculation. C_{zil} values should be assigned according to the various vegetation types, with C_{zil} decreasing with increasing canopy height, and C_h should increase through enhancement of the energy and moisture exchange efficiency, which affects the atmospheric lower boundary conditions (Chen et al. 2019;

Table 2 Differences in precipitation (Precip), surface exchange coefficient (C_h at a log10 scale), near-surface air temperature (T_a), land surface temperature (T_s), land–air temperature contrast (ΔT), 2-m specific humidity (Q), sensible heat flux (SH), latent heat flux (LH), 10-m u/v-wind components (U10/V10), u/v-wind moisture fluxes vertically integrated from 1000 to 300 hPa (IUQ/IVQ), planetary boundary layer height (PBLH), and convective available potential energy (CAPE) between the simulations involving the default M–O, $C_{zil}=0.1$, and C_{zil}-h schemes in the four typical climate zones (the blue rectangles in Fig. 1b) from 2003 to 2012

	Northeast China		North China		Eastern Northwest China		Southwest China	
	Spring ND (NC)	Summer ND (NC)	Spring ND (NC)	Summer ND (NC)	Spring ND (NC)	Summer ND (NC)	Spring ND (NC)	Summer ND (NC)
Precip (mm day^{-1})	0.06* (−0.03)	−0.38* (−0.41*)	0.05* (0.03)	−0.44* (−0.65*)	0.04 (0.02)	−0.29* (−0.02)	0.03 (−0.02)	−0.32* (−0.51*)
lg (C_h)	−0.21* (0.04)	−0.25* (0.05)	−0.25* (−0.08*)	−0.23* (−0.07*)	−0.18* (−0.12*)	−0.20* (−0.13*)	0.06* (0.24*)	−0.09* (0.26*)
T_a (°C)	−0.17* (−0.15*)	−0.20* (−0.11*)	−0.44* (−0.33*)	−0.20* (−0.20*)	−0.37* (−0.25*)	−0.26* (−0.42*)	−0.12* (−0.03)	−0.06 (−0.28*)
T_s (°C)	0.80* (−0.01)	1.01* (0.55*)	1.02* (0.42*)	1.39* (0.82*)	1.32* (0.97*)	1.50* (0.85*)	0.30* (−0.76*)	1.25* (0.87*)
$_{\Delta}$T (°C)	0.98* (0.14*)	1.20* (0.65*)	1.47* (0.75*)	1.58* (1.02*)	1.69* (1.22*)	1.76* (1.27*)	0.42* (-0.73*)	1.30* (1.15*)
Q (g kg^{-1})	0.04* (−0.06*)	0.01 (−0.12*)	0.04* (0.02)	−0.23* (−0.42*)	0.10* (0.07*)	−0.12* (−0.03)	−0.06 (−0.11*)	−0.20* (−0.08)
SH (W m^{-2})	−4.40* (1.68*)	−0.37* (2.03*)	−7.12* (−3.14*)	−5.56* (−2.82*)	−8.73* (−6.42*)	−10.37* (−7.83*)	−1.63* (8.48*)	0.03 (3.55*)
LH (W m^{-2})	1.41* (−1.44*)	−6.36* (−4.78*)	1.60* (0.95*)	−5.21* (−5.22*)	2.51* (1.86*)	−0.16 (1.99*)	−0.99* (−3.92*)	−2.82* (0.33*)
U10 (m s^{-1})	0.02 (0.06*)	−0.01 (−0.01)	−0.004 (0.02)	0.04* (0.08*)	−0.05* (−0.05*)	−0.02 (−0.04*)	−0.02 (0.03)	−0.04 (0.01)
V10 (m s^{-1})	0.01 (0.01)	0.02 (0.04*)	0.01 (−0.01)	0.05* (0.04*)	−0.01 (−0.01)	0.03 (−0.01)	−0.004 (0.01)	−0.01 (0.01)
IUQ (kg (m s)$^{-1}$)	0.20 (0.19)	−1.08 (−3.67*)	0.10 (0.31)	2.96* (0.75)	0.58* (0.81*)	−1.31* (-0.37)	0.30 (1.14)	−0.67 (2.31*)
IVQ (kg (m s)$^{-1}$)	0.03 (−0.07)	1.64* (1.51)	−0.27 (−0.23)	−0.72 (−0.12)	−0.58* (−0.18)	2.79* (0.12)	0.49 (1.86*)	−0.41 (1.42)
PBLH (m)	−0.71 (9.19*)	−0.07 (12.57*)	5.99 (5.35)	16.71* (26.28*)	9.56* (7.96*)	49.22* (34.33*)	−2.22 (15.35*)	7.78* (− 0.03)
CAPE (J kg^{-1})	−0.17 (−1.10*)	11.13* (7.71*)	−1.15* (-0.93)	−10.89* (−38.24*)	1.13 (−0.15)	−2.55 (4.45)	−7.73* (− 6.06*)	−25.22* (−18.33*)

ND denotes the mean deviation between the C_{zil}-h and default M–O simulations, and NC denotes the mean deviation between the C_{zil}-h and $C_{zil}=0.1$ simulations

*Indicates significant values at a 95% confidence level

Trier et al. 2011; Zheng et al. 2015). The coupling strength of tall vegetation canopies with rougher surfaces is 10 times higher than that of low vegetation (Chen and Zhang 2009). However, the C_{zil} value changes little in areas with canopy heights > 5 m. For example, the C_{zil} difference within the canopy height range from 19 to 20 m is only 1.51×10^{-8}, but the difference reaches 0.24 within the canopy height range from 1−2 m. A close-to-zero C_{zil} values for high vegetation results in equivalent aerodynamic and thermal roughness lengths according to Eqs. (6), (7). Therefore, the C_{zil}-h scheme produced a positive deviation similar to the default M–O scheme.

In fact, there remain many deficiencies in applying the C_{zil}-h scheme to atmospheric coupling models in regional climate simulation. First, regarding the canopy height and Z_{om}, which played important roles in the experiments, we adopted default Moderate Resolution Imaging Spectroradiometer (MODIS) land-cover classification data in the model due to the unavailability of observations across China. However, choosing Sud and Smith (1985) as an example, it was indicated that a decrease in surface roughness from 45 to 0.02 cm considerably reduced precipitation in the Sahara Desert, and the impact was comparable to that of surface albedo enhancement. Therefore, more accurate data employed in the C_{zil}-h scheme can contribute C_h parameterization improvement and can provide more valuable detailed information. Second, the C_{zil}-h scheme improved the land–atmosphere coupling strength mainly in regard to

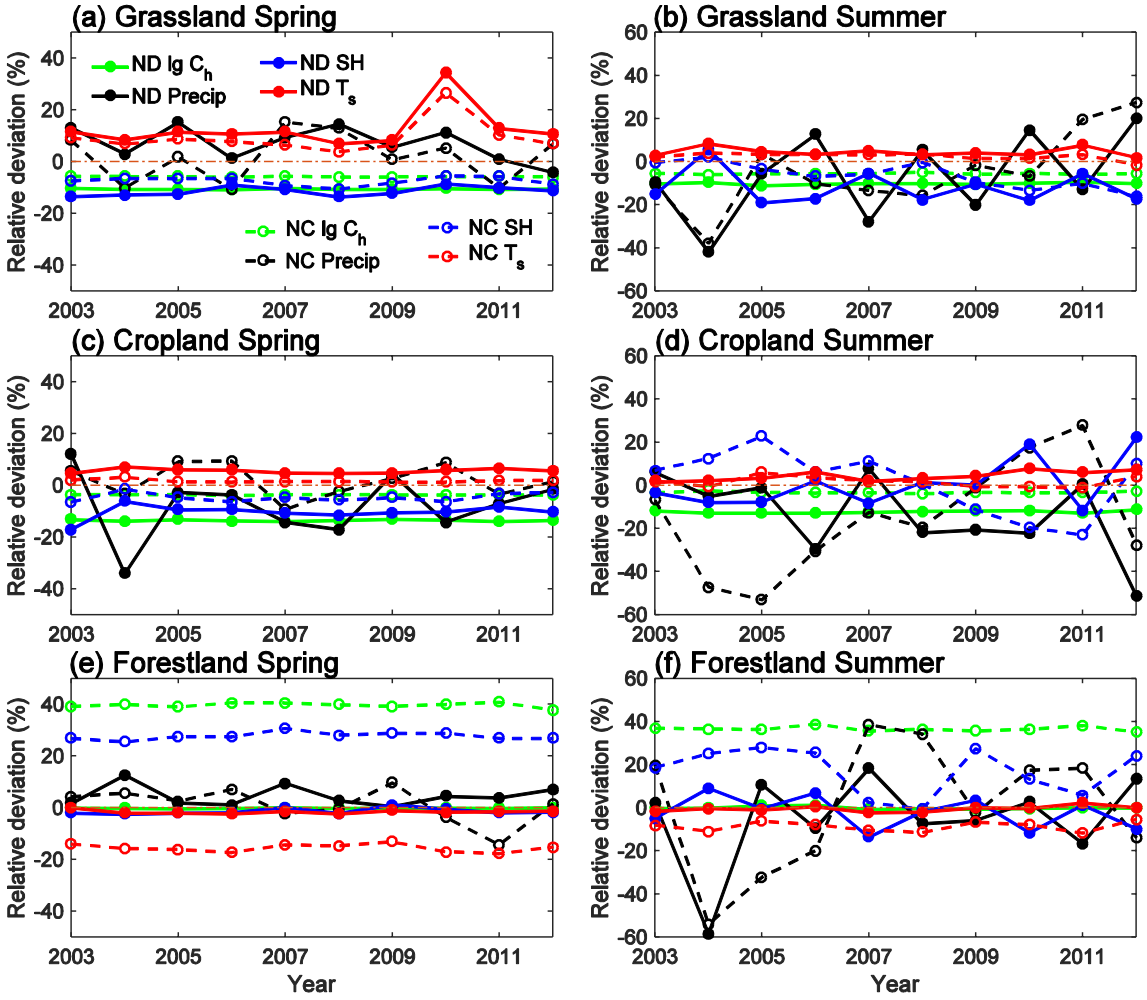

Fig. 14 Deviations in C_h (plotted at a log10 scale), sensible heat flux (SH), precipitation (Precip), and land surface temperature (T_s) between the simulations using the default M–O (Default), $C_{zil}=0.1$ (Czil), and C_{zil}-h (Newczil) schemes in **a**, **b** grassland, **c**, **d** cropland, and **e**, **f** forestland areas from 2003 to 2012. ND: (Newczil – Default)/|Newczil|× 100, NC: (Newczil – Czil)/|Newczil|× 100

short vegetation canopies, and the simulations considering high vegetation were similar to those with the default M–O scheme. Comparatively, the $C_{zil}=0.1$ scheme produced more similar C_h values to the observations. Therefore, based on extensive evaluation of the C_{zil}-h simulation results, it may be necessary to consider further improvement and optimization of the C_{zil}-h scheme in future studies. Additionally, adjustment of land–surface physical processes can substantially affect climate change (Maynard and Royer 2004; Pielke 2001; Trier et al. 2011). Moreover, changes in surface water and energy processes can result from land–surface feedbacks to atmospheric anomalies (Findell and Eltahir 2003; Wang and Zeng 2011). Thorough exploration of the differences in land–atmosphere responses and feedbacks between the various C_{zil} schemes could help to better explain the impacts of C_{zil} on the land surface and atmosphere and could contribute to C_{zil}-h scheme improvement.

4.2 Impacts and uncertainties in atmospheric dynamics on the representation of the land–atmosphere coupling strength

The representation of land–atmosphere coupling in the WRF/Noah-MP model by adjusting C_{zil} based on the vegetation type can be improved, and regional climate simulations can subsequently be modified (Sect. 3.4). Furthermore, near-surface atmospheric dynamic conditions, by influencing surface roughness elements and aerodynamic properties, interact with dynamic changes in the land–atmosphere coupling strength (C_h) in a complicated manner (Rigden et al. 2018; Zhang et al. 2012). Therefore, this section analyzes the effect of atmospheric dynamics on C_h, which in turn impacts climate simulations, and examines the influence of uncertainties in atmospheric dynamics on the representation of land–atmosphere coupling in numerical models.

Table 3 Differences in surface exchange coefficient (C_h at a log10 scale), precipitation (Precip), sensible heat flux (SH), and land surface temperature (T_s) between the simulations involving the default M–O (Default), $C_{zil}=0.1$ (Czil), and C_{zil}-h (Newczil) schemes in grassland, cropland, and forestland areas from 2003–2012

			lg (C_h)	Precip (mm day^{-1})	SH (W m^{-2})	T_s (°C)
Grassland	ND_AD (ND_RD)	Spring	− 10.58% (− 0.21*)	6.70% (0.12*)	− 11.45% (− 7.57*)	12.70% (0.90*)
		Summer	− 10.18% (− 0.21*)	− 6.50% (− 0.10*)	− 11.99% (− 7.03*)	4.44% (1.17*)
	NC_AD (NC_RD)	Spring	− 5.83% (− 0.12*)	1.96% (0.07)	− 7.49% (− 4.96*)	9.30% (0.65*)
		Summer	− 5.57% (− 0.11*)	− 4.55% (− 0.03*)	− 6.42% (− 3.78*)	2.46% (0.65*)
Cropland	ND_AD (ND_RD)	Spring	− 13.56% (− 0.25*)	− 7.84% (− 0.05*)	− 10.37% (− 5.96*)	5.62% (0.97*)
		Summer	− 12.29% (− 0.24*)	− 13.77% (− 0.61*)	1.55% (1.71)	4.38% (1.27*)
	NC_AD (NC_RD)	Spring	− 3.66% (− 0.06*)	1.84% (0.03)	− 4.70% (− 2.69*)	1.71% (0.30)
		Summer	− 3.30% (− 0.06*)	− 15.33% (− 0.84*)	1.59% (1.40)	1.60% (0.47)
Forestland	ND_AD (ND_RD)	Spring	− 0.15% (− 0.002)	4.52% (0.19*)	− 1.38% (− 0.78)	− 1.57% (− 0.17)
		Summer	− 0.03% (− 0.001)	− 5.05% (0.16*)	− 2.19% (− 0.35)	− 0.47% (− 0.09)
	NC_AD (NC_RD)	Spring	39.68% (0.52*)	1.00% (0.09)	27.70% (15.84*)	− 15.56% (− 1.64*)
		Summer	36.55% (0.50*)	1.55% (0.59)	16.94% (7.75*)	− 8.68% (− 1.93*)

ND_AD (NC_AD) denotes the absolute deviation between the C_{zil}-h and default M–O ($C_{zil}=0.1$) schemes, i.e., ND_AD = Newczil—Default, NC_AD = Newczil—Czil; ND_RD (NC_RD) denotes the relative deviation between the C_{zil}-h and default M–O ($C_{zil}=0.1$) schemes, i.e., ND_RD = (Newczil – Default)/|Newczil|× 100, NC_RD = (Newczil—Czil)/|Newczil|× 100

*Indicates significant absolute deviation values at a 95% confidence level

In this study, we referred to Zhang et al. (2012) to construct a dynamic comprehensive variable $u^2/u*$, in which the surface wind speed (u) considerably changes the structure and morphology of roughness elements (e.g., the plant height and density), while the friction velocity ($u*$) can represent the interaction between near-surface airflow and roughness elements (Rigden et al. 2018; Zilitinkevich et al. 2008). Moreover, the M–O stability parameter ζ (the calculation is described in Sect. 2.1), which comprehensively considers the thermodynamic influences on atmospheric stability and functions as a determinant in C_h parameterization (Grachev et al. 1998; Yang et al. 2001), was analyzed. Figure 15 shows scatter plots between C_h and $u^2/u*$, ζ and precipitation simulated with the C_{zil}-h scheme in grassland, cropland, and forestland areas (the coverage is equivalent to that mentioned in Sect. 4.1). The correlations between C_h and $u^2/u*$ are significantly positive ($p<0.05$) in the three vegetation regions, indicating enhanced effects of airflow movement on surface exchange processes. The C_h and $u^2/u*$ values in forestlands attain a higher correlation coefficient value of 0.64 than those in grasslands and croplands (~0.4), suggesting that C_h of high vegetation canopies is highly susceptible to atmospheric dynamic conditions. The scatter points between C_h and $u^2/u*$ are highly dispersed in grasslands and croplands, whereas in forestlands, the variations in $u^2/u*$ are more concentrated presumably due to the decrease in surface wind speed resulting from the blocking effect of dense canopies (Maynard and Royer 2004; Pielke 2001). Thus, the climatic average $u^2/u*$ values in the forestland areas (55.98 m s^{-1}) are lower than those in the grassland (90.23 m s^{-1}) and cropland areas (85.51 m s^{-1}), despite the larger C_h values in the forestland areas (an average lg(C_h) value of − 1.61) than those in the cropland (− 2.01) and grassland (− 2.08) areas. C_h and ζ are negatively correlated. ζ mostly yields negative values, denoting unstable atmospheric stratification ($\zeta<-0$ 0.01), and the larger the value of |ζ|, the higher the instability. Accordingly, the coupling strength increase (larger C_h values). As the atmosphere stabilizes ($\zeta>0$ 0.01), C_h tends to decrease and the land–atmosphere coupling strength weakens, while $-0.01<\zeta<0.01$ indicates a near-neutral atmosphere. The atmosphere over forestland areas exhibits the highest instability with a broader |ζ| range from 0–1.5 × 10^4, leading to the most efficient land–atmosphere coupling with a lg(C_h) range from − 2.6 to − 0.8. However, the lowest atmospheric instability occurs in grassland areas, with sparse values of |ζ| over 10^4, which are smaller than those in forestland and cropland areas, thus corresponding to a modest coupling strength. The C_h and precipitation values are relatively dispersed but still exhibit significant positive correlations ($p<0.05$). The enhanced coupling strength due to an increase in C_h through heat and water exchange facilitates precipitation increase. Moreover, sufficient rainfall enables vegetation to flourish, which in turn increases C_h by affecting the surface roughness (Chen and Zhang 2009; Zhang et al. 2013).

The complicated interactions between atmospheric dynamic conditions and land–atmosphere coupling strength variability result in challenges in the accurate characterization of land–atmosphere interactions in numerical models. The influences of atmospheric dynamics on land–surface

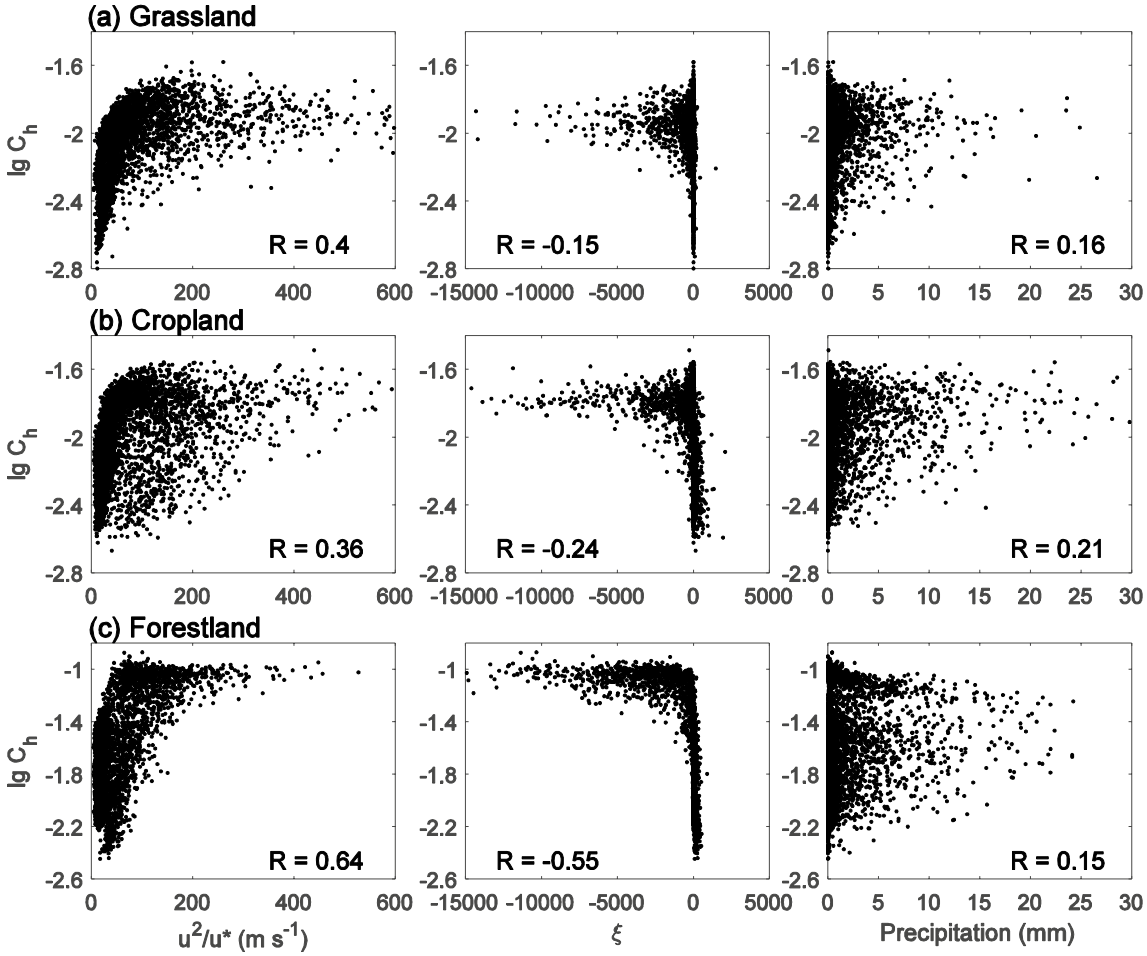

Fig. 15 Scatter plots for **a** grassland, **b** cropland, and **c** forestland areas between the 6-hourly C_h (plotted at a log10 scale) and the dynamic comprehensive variable (u^2/u^*), Monin–Obukhov stability parameter (ζ) and precipitation simulated with the C_{zil}-h scheme in summer from 2003 to 2012. u^2/u^* is the ratio of the surface wind speed (u) squared and friction velocity (u^*), and ζ is the ratio of the reference height and Monin–Obukhov length (the detailed calculation expressed as Eq. (5)). The Pearson correlation coefficient between the simulations and observations (R) is displayed in each panel

processes are closely connected not only to the surface roughness geometry, such as the plant height and density, but also to the dynamic responses of vegetation to airflow (e.g., the flexibility of crops and grass). However, the intricate processes of dynamic roughness changes affecting C_h have yet to be implemented in current models (Gomez et al. 2020; Zhang et al. 2012; Zilitinkevich et al. 2008). Moreover, the variations in Z_{om}, a key factor influencing C_h parameterization, are manifested due to the notable dependence of vegetation growth on the precipitation variability (Zhang et al. 2013). In contrast, the Z_{om} values in this study were determined as a function of only the vegetation type, similar to the approach in most current numerical models (e.g., Trier et al. (2011)), and thus, the introduction of dynamic Z_{om} data (e.g., monthly values) in the model may improve the simulation results.

5 Conclusions

In this study, we investigated the sensitivity of regional climate simulations over China from 2003 to 2012 to the parametrization of land–atmosphere coupling in a 13-km resolution WRF/Noah-MP model. The surface coupling strength in the model was greatly affected by parameter C_{zil}, which is typically defined as a constant, through dynamic adjustment based on the land-cover type. Thus, we designed three C_{zil} schemes, namely, default M–O ($C_{zil} \sim 0$), constant C_{zil} (set to 0.1) and dynamic canopy-height-dependent C_{zil} (C_{zil}-h) schemes, and the simulations were compared to observations retrieved from more than 2000 meteorological stations and eight ChinaFLUX sites. The main conclusions of this study are summarized as follows.

The remarkable differences in land–atmosphere coupling strength can be modeled with the three C_{zil} schemes.

The default M–O scheme substantially overestimates the observation-derived C_h, while the $C_{zil}=0.1$ scheme slightly reduces the positive deviation. In contrast, the C_{zil}-h scheme produces the lowest C_h deviation from the observations in regard to short vegetation canopies (e.g., cropland, grassland, and shrubland areas) and yields C_h values similar to those calculated with the default M–O scheme in regard to high canopies (e.g., mixed forestland areas). Additionally, a comparison to ChinaFLUX observations indicates the capability of the C_{zil}-h scheme in yielding a better match to the observed surface energy and water variations. In general, application of the C_{zil}-h scheme can achieve improved representation of land–atmosphere coupling in numerical models.

C_{zil} adjustment with the vegetation type can modulate the exchange efficiency of land–atmosphere energy and moisture and subsequently alter regional climate simulations through the atmospheric planetary boundary layer. The results obtained through the application of the various C_{zil} schemes in four typical climate zones in China indicate that the C_{zil}-h simulations attain the closest agreement with the field observations. The C_{zil}-h scheme narrows the positive discrepancies in the simulated precipitation and surface fluxes and the negative biases of T_s in Northeast China, North China, eastern Northwest China, and Southwest China over the default M–O and $C_{zil}=0.1$ schemes. This occurs because the C_{zil}-h scheme, through mitigation of the land–surface coupling efficiency, transfers lower surface fluxes into the atmosphere and correspondingly increases T_s. The elevated PBLH simulated with the C_{zil}-h scheme enhances water vapor mixing in the lower atmosphere, in addition to greater moisture evaporation due to a higher T_s, resulting in a notable reduction in near-surface humidity. The decreased precipitation in the C_{zil}-h experiments is associated with horizontal transport of less water vapor from moisture source areas, evaporation of less moisture from drier surfaces, thus vertically weakening LH, and lower atmosphere stabilization and thermal convection suppression attributed to CAPE reduction.

Although the C_{zil}-h scheme achieves a competitive skill in representing land–atmosphere coupling, the deficiencies and uncertainties in the application of the dynamic C_{zil}-h scheme in atmospheric coupled models, e.g., the accuracy of canopy height and Z_{om} data, regional scheme applicability, and dynamic responses of vegetation to airflow, must be further explored and resolved by performing a large number of experiments. These efforts may be helpful in accurately characterizing land–atmosphere coupling and further optimizing C_h parameterization. Additionally, using a convection-permitting model to further explore the impacts of different coupling strengths on precipitation simulations will be the focus of our future work.

Acknowledgements This work was funded by the Strategic Priority Research Program of the Chinese Academy of Sciences (Grant Number: XDA23040501), the National Natural Science Foundation of China (Grant Number: 41875116), and the National Key Scientific and Technological Infrastructure project "Earth System Science Numerical Simulator Facility" (EarthLab). We acknowledge the use of the meteorological station data provided by the China Meteorological Administration (http://data.cma.cn/), the ChinaFLUX observation data from the FLUXNET network (http://www.fluxdata.org), and the FLUXNET model tree ensembles (MTE) products from the Max Planck Institute for Biogeochemistry (http://www.bgc-jena.mpg.de/geodb/).

Declarations

Conflict of interest There are no conflicts of interest to declare.

References

Allen RG, Pereira LS, Raes D Smith M (1998) Crop evaporation guidelines for computing crop water requirements. FAO-Food and Agriculture Organization of the United Nations. Irrigation and drainage. Rome, p 56

Atlas R, Wolfson N, Terry J (1993) The effect of SST and soil-moisture anomalies on GLA model simulations of the 1988 united-states summer drought. J Clim 6(11):2034–2048. https://doi.org/10.1175/1520-0442(1993)006%3c2034:teosas%3e2.0.co;2

Beljaars ACM, Viterbo P (1994) The sensitivity of winter evaporation to the formulation of aerodynamic resistance in the ECMWF model. Bound-Layer Meteorol 71(1–2):135–149. https://doi.org/10.1007/bf00709223

Betts AK, Ball JH, Beljaars ACM, Miller MJ, Viterbo PA (1996) The land surface-atmosphere interaction: a review based on observational and global modeling perspectives. J Geophys Res Atmos 101(D3):7209–7225. https://doi.org/10.1029/95jd02135

Bonan GB et al (2011) Improving canopy processes in the Community Land Model version 4 (CLM4) using global flux fields empirically inferred from FLUXNET data. J Geophys Res Biogeosci 116(G2):1–22. https://doi.org/10.1029/2010JG001593

Brovkin V, Boysen L, Raddatz T, Gayler V, Loew A, Claussen M (2013) Evaluation of vegetation cover and land-surface albedo in MPI-ESM CMIP5 simulations. J Adv Model Earth Syst 5(1):48–57. https://doi.org/10.1029/2012ms000169

Brutsaert WA (1982) Evaporation into the atmosphere: theory, history and applications. D. Reidel, Dordrecht, Netherlands: Cornell University, pp 299. https://doi.org/10.1007/978-94-017-1497-6

Chen F, Zhang Y (2009) On the coupling strength between the land surface and the atmosphere: from viewpoint of surface exchange coefficients. Geophys Res Lett 36(10):1–5. https://doi.org/10.1029/2009gl037980

Chen F et al (1996) Modeling of land surface evaporation by four schemes and comparison with FIFE observations. J Gerontol Ser A Biol Med Sci 101(D3):7251–7268. https://doi.org/10.1029/95jd02165

Chen F, Janjic Z, Mitchell K (1997) Impact of atmospheric surface-layer parameterizations in the new land-surface scheme of the NCEP mesoscale Eta model. Bound-Layer Meteorol 85(3):391–421. https://doi.org/10.1023/a:1000531001463

Chen F et al (2007) Description and evaluation of the characteristics of the NCAR high-resolution land data assimilation system. J Appl Meteorol Climatol 46(6):694–713. https://doi.org/10.1175/jam2463.1

Chen YY, Yang K, Zhou DG, Qin J, Guo XF (2010) Improving the NOAH land surface model in arid regions with an appropriate parameterization of the thermal roughness length. J

Hydrometeorol 11(4):995–1006. https://doi.org/10.1175/2010jhm1185.1
Chen YY, Yang K, He J, Qin J, Shi JC, Du JY, He Q (2011) Improving land surface temperature modeling for dry land of China. J Gerontol Ser A Biol Med Sci 116(D20):1–15. https://doi.org/10.1029/2011jd015921
Chen L, Li YP, Chen F, Barlage M, Zhang Z, Li ZH (2019) Using 4-km WRF CONUS simulations to assess impacts of the surface coupling strength on regional climate simulation. Clim Dyn 53(9–10):6397–6416. https://doi.org/10.1007/s00382-019-04932-9
Dai YJ et al (2019) A global high-resolution data set of soil hydraulic and thermal properties for land surface modeling. J Adv Model Earth Syst 11(9):2996–3023. https://doi.org/10.1029/2019ms001784
Dee DP et al (2011) The ERA-Interim reanalysis: configuration and performance of the data assimilation system. Q J R Meteorol Soc 137(656):553–597. https://doi.org/10.1002/qj.828
Dirmeyer PA, Koster RD, Guo ZC (2006) Do global models properly represent the feedback between land and atmosphere? J Hydrometeorol 7(6):1177–1198. https://doi.org/10.1175/jhm532.1
Findell KL, Eltahir EAB (2003) Atmospheric controls on soil moisture-boundary layer interactions. Part II: feedbacks within the continental United States. J Hydrometeorol 4(3):570–583. https://doi.org/10.1175/1525-7541(2003)004%3c0570:acosml%3e2.0.co;2
Gan Y, Liang XZ, Duan Q, Chen F, Li J, Zhang Y (2019) Assessment and reduction of the physical parameterization uncertainty for Noah-MP land surface model. Water Resour Res 55(7):5518–5538. https://doi.org/10.1029/2019wr024814
Gao Y, Chen F, Jiang Y (2020) Evaluation of a convection-permitting modeling of precipitation over the Tibetan Plateau and its influences on the simulation of snow-cover fraction. J Hydrometeorol 21(7):1531–1548. https://doi.org/10.1175/jhm-d-19-0277.1
Garratt JR (1992) The atmospheric boundary layer. Cambridge University Press, New York, p 316
Goff JA (1957) Saturation pressure of water on the new Kelvin temperature scale, transactions of the american society of heating and ventilating engineers. General Books LLC, pp 347–354
Gomez I, Caselles V, Estrela MJ (2020) Improving RAMS and WRF mesoscale forecasts over two distinct vegetation covers using an appropriate thermal roughness length parameterization. Agric for Meteorol 280:1–11. https://doi.org/10.1016/j.agrformet.2019.107791
Grachev AA, Fairall CW, Larsen SE (1998) On the determination of the neutral drag coefficient in the convective boundary layer. Bound-Layer Meteorol 86(2):257–278. https://doi.org/10.1023/a:1000617300732
Högström U (1967) Turbulent water-vapor transfer at different stability conditions. Phys Fluids 10(9):S247–S254. https://doi.org/10.1063/1.1762460
Hong SY, Noh Y, Dudhia J (2006) A new vertical diffusion package with an explicit treatment of entrainment processes. Mon Weather Rev 134(9):2318–2341. https://doi.org/10.1175/mwr3199.1
Houze RA (2012) Orographic effects on precipitating clouds. Rev Geophys 50(1):1–47. https://doi.org/10.1029/2011rg000365
Huang Y et al (2016) Effects of roughness length parameterizations on regional-scale land surface modeling of alpine grasslands in the Yangtze river basin. J Hydrometeorol 17(4):1069–1085. https://doi.org/10.1175/jhm-d-15-0049.1
Huang J et al (2017) Dryland climate change: recent progress and challenges. Rev Geophys 55(3):719–778. https://doi.org/10.1002/2016rg000550
Hulme M (1996) Recent climatic change in the World's drylands. Geophys Res Lett 23(1):61–64. https://doi.org/10.1029/95gl03586
Huo F, Jiang Z, Ma H, Li Z, Li Y (2021) Reduction in autumn precipitation over Southwest China by anthropogenic aerosol emissions from eastern China. Atmos Res 257:1–12. https://doi.org/10.1016/j.atmosres.2021.105627
Iacono MJ, Delamere JS, Mlawer EJ, Shephard MW, Clough SA, Collins WD (2008) Radiative forcing by long-lived greenhouse gases: calculations with the AER radiative transfer models. J Gerontol Ser A Biol Med Sci 113(D13):1–8. https://doi.org/10.1029/2008jd009944
Jung M, Reichstein M, Bondeau A (2009) Towards global empirical upscaling of FLUXNET eddy covariance observations: validation of a model tree ensemble approach using a biosphere model. Biogeosciences 6(10):2001–2013. https://doi.org/10.5194/bg-6-2001-2009
Kain JS (2004) The Kain–Fritsch convective parameterization: an update. J Appl Meteorol 43(1):170–181. https://doi.org/10.1175/1520-0450(2004)043%3c0170:tkcpau%3e2.0.co;2
Koster RD, Suarez MJ, Higgins RW, Van den Dool HM (2003) Observational evidence that soil moisture variations affect precipitation. Geophys Res Lett 30(5):1–4. https://doi.org/10.1029/2002gl016571
Koster RD et al (2004) Regions of strong coupling between soil moisture and precipitation. Science 305(5687):1138–1140. https://doi.org/10.1126/science.1100217
Kurkute S, Li Z, Li Y, Huo F (2020) Assessment and projection of the water budget over western Canada using convection-permitting weather research and forecasting simulations. Hydrol Earth Syst Sci 24(7):3677–3697. https://doi.org/10.5194/hess-24-3677-2020
LeMone MA, Tewari M, Chen F, Alfieri JG, Niyogi D (2008) Evaluation of the Noah land surface model using data from a fair-weather IHOP_2002 day with heterogeneous surface fluxes. Mon Weather Rev 136(12):4915–4941. https://doi.org/10.1175/2008mwr2354.1
Li MX, Ma ZG, Gu HP, Yang Q, Zheng ZY (2017) Production of a combined land surface data set and its use to assess land-atmosphere coupling in China. J Geophys Res Atmos 122(2):948–965. https://doi.org/10.1002/2016JD025511
Li Z, Li Y, Bonsal B, Manson AH, Scaff L (2018) Combined impacts of ENSO and MJO on the 2015 growing season drought on the Canadian Prairies. Hydrol Earth Syst Sci 22(10):5057–5067. https://doi.org/10.5194/hess-22-5057-2018
Li YP, Li ZH, Zhang Z, Chen L, Kurkute S, Scaff L, Pan XC (2019) High-resolution regional climate modeling and projection over western Canada using a weather research forecasting model with a pseudo-global warming approach. Hydrol Earth Syst Sci 23(11):4635–4659. https://doi.org/10.5194/hess-23-4635-2019
Lian X, Zeng Z, Yao Y, Peng S, Wang K, Piao S (2017) Spatiotemporal variations in the difference between satellite-observed daily maximum land surface temperature and station-based daily maximum near-surface air temperature. J Geophys Res Atmos 122(4):2254–2268. https://doi.org/10.1002/2016JD025366
Liu CH et al (2017) Continental-scale convection-permitting modeling of the current and future climate of North America. Clim Dyn 49(1–2):71–95. https://doi.org/10.1007/s00382-016-3327-9
Los SO, Weedon GP, North PRJ, Kaduk JD, Taylor CM, Cox PM (2006) An observation-based estimate of the strength of rainfall-vegetation interactions in the Sahel. Geophys Res Lett 33(16):1–5. https://doi.org/10.1029/2006gl027065
Ma Z, Fu C (2003) Interannual characteristics of the surface hydrological variables over the arid and semi-arid areas of northern China. Global Planet Change 37(3):189–200. https://doi.org/10.1016/S0921-8181(02)00203-5
Maynard K, Royer JF (2004) Sensitivity of a general circulation model to land surface parameters in African tropical deforestation experiments. Clim Dyn 22(6–7):555–572. https://doi.org/10.1007/s00382-004-0398-9

Middleton NJ, Thomas DS (1992) World atlas of desertification. Edward Arnold

Mildrexler DJ, Zhao M, Running SW (2011) A global comparison between station air temperatures and MODIS land surface temperatures reveals the cooling role of forests. J Geophys Res Biogeosci 116(G3):1–15. https://doi.org/10.1029/2010JG001486

Molod A, Salmun H, Dempsey M (2015) Estimating planetary boundary layer heights from NOAA profiler network wind profiler data. J Atmos Oceanic Tech 32(9):1545–1561. https://doi.org/10.1175/jtech-d-14-00155.1

Niu GY et al (2011) The community Noah land surface model with multiparameterization options (Noah-MP): 1. Model description and evaluation with local-scale measurements. J Geophys Res-Atmos 116(D12109):1–19. https://doi.org/10.1029/2010jd015139

Paulson CA (1970) The mathematical representation of wind speed and temperature profiles in the unstable atmospheric surface layer. J Appl Meteorol 9(6):857–861. https://doi.org/10.1175/1520-0450(1970)009%3c0857:tmrows%3e2.0.co;2

Pielke RA (2001) Influence of the spatial distribution of vegetation and soils on the prediction of cumulus convective rainfall. Rev Geophys 39(2):151–177. https://doi.org/10.1029/1999rg000072

Reijmer CH, Van Meijgaard E, Van Den Broeke MR (2004) Numerical studies with a regional atmospheric climate model based on changes in the roughness length for momentum and heat over Antarctica. Bound-Layer Meteorol 111(2):313–337. https://doi.org/10.1023/B:BOUN.0000016470.23403.ca

Rigden A, Li D, Salvucci G (2018) Dependence of thermal roughness length on friction velocity across land cover types: a synthesis analysis using AmeriFlux data. Agric for Meteorol 249:512–519. https://doi.org/10.1016/j.agrformet.2017.06.003

Ruiz-Barradas A, Nigam S (2005) Warm season rainfall variability over the US Great Plains in observations, NCEP and ERA-40 Reanalyses, and NCAR and NASA atmospheric model simulations. J Clim 18(11):1808–1830. https://doi.org/10.1175/jcli3343.1

Seneviratne SI et al (2010) Investigating soil moisture-climate interactions in a changing climate: a review. Earth Sci Rev 99(3–4):125–161. https://doi.org/10.1016/j.earscirev.2010.02.004

Siemann AL, Chaney N, Wood EF (2018) Sensitivity and uncertainty of a long-term, high-resolution, global, terrestrial sensible heat flux data set. J Gerontol Ser A Biol Med Sci 123(10):4988–5000. https://doi.org/10.1029/2017jd027785

Skamarock WC et al (2008) A description of the advanced research WRF Version 3. NCAR Technical Note NCAR/TN-475 + STR. https://doi.org/10.5065/D68S4MVH

Song JH, Kang HS, Byun YH, Hong SY (2010) Effects of the Tibetan Plateau on the Asian summer monsoon: a numerical case study using a regional climate model. Int J Climatol 30(5):743–759. https://doi.org/10.1002/joc.1906

Sud YC, Smith WE (1985) The influence of surface-roughness of deserts on the July circulation (a numerical study). Bound-Layer Meteorol 33(1):15–49. https://doi.org/10.1007/bf00137034

Swinbank WC, Dyer AJ (1967) An experimental study in micro-meteorology. Q J R Meteorol Soc 93(398):494–500. https://doi.org/10.1002/qj.49709339808

Thompson G, Field PR, Rasmussen RM, Hall WD (2008) Explicit forecasts of winter precipitation using an improved bulk microphysics scheme. Part II: Implementation of a new snow parameterization. Monthly Weather Rev 136(12):5095–5115. https://doi.org/10.1175/2008mwr2387.1

Trenberth KE (1999) Atmospheric moisture recycling: role of advection and local evaporation. J Clim 12(5):1368–1381. https://doi.org/10.1175/1520-0442(1999)012%3c1368:amrroa%3e2.0.co;2

Trenberth KE, Guillemot CJ (1996) Physical processes involved in the 1988 drought and 1993 floods in North America. J Clim 9(6):1288–1298. https://doi.org/10.1175/1520-0442(1996)009%3c1288:ppiitd%3e2.0.co;2

Trier SB, Chen F, Manning KW (2004) A study of convection initiation in a mesoscale model using high-resolution land surface initial conditions. Mon Weather Rev 132(12):2954–2976. https://doi.org/10.1175/mwr2839.1

Trier SB, LeMone MA, Chen F, Manning KW (2011) Effects of surface heat and moisture exchange on ARW-WRF warm-season precipitation forecasts over the central United States. Weather Forecast 26(1):3–25. https://doi.org/10.1175/2010waf2222426.1

Wang AH, Zeng XB (2011) Sensitivities of terrestrial water cycle simulations to the variations of precipitation and air temperature in China. J Gerontol Ser A Biol Med Sci 116:11. https://doi.org/10.1029/2010jd014659

Wang ZQ, Duan AM, Wu GX (2014) Time-lagged impact of spring sensible heat over the Tibetan Plateau on the summer rainfall anomaly in East China: case studies using the WRF model. Clim Dyn 42(11–12):2885–2898. https://doi.org/10.1007/s00382-013-1800-2

Wang J, Feng JM, Yan ZW (2015) Potential sensitivity of warm season precipitation to urbanization extents: modeling study in Beijing–Tianjin–Hebei urban agglomeration in China. J Gerontol Ser A Biol Med Sci 120(18):9408–9425. https://doi.org/10.1002/2015jd023572

Yang K, Tamai N, Koike T (2001) Analytical solution of surface layer similarity equations. J Appl Meteorol 40(9):1647–1653. https://doi.org/10.1175/1520-0450(2001)040%3c1647:asosls%3e2.0.co;2

Yang K et al (2008) Turbulent flux transfer over bare-soil surfaces: characteristics and parameterization. J Appl Meteorol Climatol 47(1):276–290. https://doi.org/10.1175/2007jamc1547.1

Yang ZL et al (2011) The community Noah land surface model with multiparameterization options (Noah-MP): 2. Evaluation over global river basins. J Geophys Res Atmos 116(D12110):1–16. https://doi.org/10.1029/2010jd015140

Zhang JY, Wang WC, Leung LR (2008) Contribution of land-atmosphere coupling to summer climate variability over the contiguous United States. J Gerontol Ser A Biol Med Sci 113(D22109):1–15. https://doi.org/10.1029/2008jd010136

Zhang Q, Zeng J, Yao T (2012) Interaction of aerodynamic roughness length and windflow conditions and its parameterization over vegetation surface. Chin Sci Bull 57(13):1559–1567. https://doi.org/10.1007/s11434-012-5000-y

Zhang Q, Li H, Zhang L, Yue P, Shi J (2013) Responses of the land-surface process and its parameters over the natural vegetation underlying surface of the middle of Gansu in loess plateau to precipitation fluctuation. Acta Physica Sinica 62(1):522–532. https://doi.org/10.7498/aps.62.019201

Zhang X, Li MX, Ma ZG, Yang Q, Lv MX, Clark R (2019) Assessment of an evapotranspiration deficit drought index in relation to impacts on ecosystems. Adv Atmos Sci 36(11):1273–1287. https://doi.org/10.1007/s00376-019-9061-6

Zhang Z, Li Y, Chen F, Barlage M, Li Z (2020) Evaluation of convection-permitting WRF CONUS simulation on the relationship between soil moisture and heatwaves. Clim Dyn 55(1):235–252. https://doi.org/10.1007/s00382-018-4508-5

Zhang X, Chen L, Ma Z, Gao Y (2021) Assessment of surface exchange coefficients in the Noah-MP land surface model for different land-cover types in China. Int J Climatol 41(4):2638–2659. https://doi.org/10.1002/joc.6981

Zheng Y, Kumar A, Niyogi D (2015) Impacts of land-atmosphere coupling on regional rainfall and convection. Clim Dyn 44(9–10):2383–2409. https://doi.org/10.1007/s00382-014-2442-8

Zilitinkevich SS, Mammarella I, Baklanov AA, Joffre SM (2008) The effect of stratification on the aerodynamic roughness length and displacement height. Bound-Layer Meteorol 129(2):179–190. https://doi.org/10.1007/s10546-008-9307-9

Zilitinkevich S (1995) Non-local turbulent transport: pollution dispersion aspects of coherent structure of convective flows. In: Power H, Moussiopoulos N, A. Brebbia C (eds), Air pollution III-volume I. Air pollution theory and simulation. Computational Mechanics Publications, Southampton, Boston, pp 53–60